Geometry of anisotropic contextual interactions in the visual cortex places fundamental limits on spatial vision.

Mitchell P. Morton[1,2], Sachira Denagamage[1,2], Nyomi V. Hudson[1], and Anirvan S. Nandy[1-4]

[1]Department of Neuroscience, Yale University, New Haven, CT 06510
[2]Interdepartmental Neuroscience Program, Yale University, New Haven, CT 06510
[3]Wu Tsai Institute, Yale University, New Haven, CT 06511
[4]Kavli Institute for Neuroscience, Yale University, New Haven, CT 06511

Correspondence: mitchell.morton@yale.edu, anirvan.nandy@yale.edu

ABSTRACT

A fundamental assumption underlying our understanding of how neurons in the visual cortex integrate contextual information is that contextual integrations are isotropic. However, psychophysical studies of crowding effects, the impaired ability to accurately recognize a target stimulus among distractors, suggest that interactions among stimuli are anisotropic, with distractors placed at a more eccentric point on the radial axis (termed 'radial-out crowding'), exerting the strongest impairment. We investigated how distractor stimuli in different spatial configurations impacted the representation of a target stimulus in laminar microcircuits in the primary visual cortex (V1). Our study reveals that radial-out crowding more strongly impairs stimulus representation in excitatory neurons in the superficial and input layers of V1, which represent the primary feed-forward output of the region, by a tuned suppression and untuned facilitation of orientation responses. Mechanistically, this effect can be explained by asymmetrical spatial kernels in a normalization model of cortical activity. These results underscore the non-uniform spatial integration of information by neurons in the visual cortex, establishing the presence of anisotropic contextual interactions in the earliest stages of cortical processing.

INTRODUCTION

Our ability to perceive objects in the visual world is profoundly limited by the phenomenon of visual crowding, which decreases our ability to recognize target objects among visual clutter (*1*). Crowding not only limits perception and visually guided behavior in normally sighted individuals but also impacts patients with conditions ranging from macular degeneration to dyslexia (*2*). The area in visual space over which distractor stimuli impact the perception of a central target is referred to as the crowding zone. A fundamental property of crowding zones is their anisotropy in visual space (for review, see *3*). Psychophysical studies of crowding have identified two major anisotropic characteristics of crowding in perception. First, distractor stimuli positioned on the radial axis exert a larger influence on perception than distractors on the tangential axis (*4, Figure 1A*). Second, crowding is asymmetrical along the radial axis, such that distractors that are more eccentric than the target more strongly impair perception than distractors that are less eccentric than the target (*5*). Together, these results indicate that distractor stimuli positioned on the radial axis and more eccentric than the target (radial-out crowding) are more effective at inducing crowding effects than stimuli either on the radial axis but less eccentric than the target (radial-in crowding) or on the tangential axis (tangential crowding).

Psychophysical studies have suggested that crowding emerges in the cortex (*6, 7*), and various models (*8-12*) have been proposed to explain crowding effects based on the anatomy and connectivity within the primary visual cortex (V1). Prior studies have hypothesized crowding can emerge due to properties in cortical areas V1 (*9, 13*), V2 (*14*), or V4 (*15*). Mechanistic explanations of crowding include averaging across stimuli (*16, 17*), inaccurately representing distractors as targets (*18*), or summary statistic

representations of peripheral vision (*19*). Despite these efforts, very little experimental evidence exists to validate or refute any proposed neural mechanisms. While the perceptual effects of crowding have been studied for many decades (*1, 3, 9, 20-22*), it was only recently that there has emerged direct evidence of neural correlates underlying the phenomenon (*23, 24*). The question of exactly when and how crowding effects emerge in the visual hierarchy remains unresolved, but recent work has shown that crowding impairs feature representations as early as V1 (*23, 24*). However, the neural mechanisms responsible for how the spatial geometry of stimuli affects the strength of crowding remain poorly understood at the level of cortical microcircuits composed of multiple laminae and cell classes (*25-28*).

We sought to understand how stimuli presented outside the receptive field center could influence stimulus representations in the V1 laminar microcircuit in a spatially anisotropic manner. We hypothesized that radial-out crowding would most strongly impact the representation of target stimuli among excitatory neurons in the output layers of V1. We further hypothesized that these anisotropic contextual interactions might be most prevalent in the subpopulations involved in feed-forward information propagation, particularly excitatory neurons in the input and superficial layers. These neurons play a key role in the propagation of stimulus information to higher cortical areas and are therefore critical for perception. Evidence of anisotropic impairment of stimulus representations in these neurons would upend the prevailing assumption of isotropic contextual integration and point to the neural loci of psychophysical crowding effects at these earliest stages of visual cortical processing.

RESULTS

To study how the spatial configuration of stimuli influences neural responses in area V1, we trained monkeys to perform a passive fixation task while we presented stimuli in different geometric arrangements relative to each neuron's receptive field. Monkeys fixated on the center of the screen and passively viewed stimuli presented either alone (target-only condition) or along with a distractor in one of four locations (crowding). We defined three crowding conditions based on the spatial position of the distractor relative to the target (Figure 1A, see Methods). The radial-in and radial-out crowding conditions positioned the distractor on the radial axis connecting the target to the fixation point. In the radial-in condition, the distractor was placed between the target and the fixation point, while in the radial-out condition, the distractor was past the target on the radial axis. For the tangential crowding condition, the distractor was positioned on the tangential axis (the line orthogonal to the radial axis and passing through the target) on either side of the target.

During the task, we performed laminar extracellular recordings (*29, 30*) of single unit activity in V1 through an artificial dura (Figure 1B-F, S1A-B). Probes were inserted orthogonal to the cortical surface to record from each layer along the depth of a column (Figure 1C). The receptive fields of all recording sites were well-aligned in visual space (Figure 1C). We positioned the stimuli such that the target stimulus was presented at the center of the aggregate receptive field of the recording sites. During our recordings, we collected data from 905 well-isolated single units (Figure 1E, 511 from monkey M, 394 from monkey D). We used established procedures (*29, 31-35*) to classify these neurons based on their waveform shape into broad-spiking (putative excitatory) and narrow-spiking (putative inhibitory) neurons (Figure 1E-F). Many observed differences between

broad- and narrow-spiking neurons suggest they correspond well with excitatory and inhibitory neurons respectively (*29, 32, 33, 35-39*). We used current source density (CSD) analysis to identify the superficial (II/III), input (IV), and deep (V & VI) cortical layers (*29, 40*) (Figure 1D). This allowed us to analyze the different impacts of distractor stimuli based on their spatial location in six subpopulations of the laminar cortical circuit: broad- and narrow-spiking neurons in each of the three layers. Each of these subpopulations was visually responsive and well-tuned to the orientation of the target stimulus (Figure S2A-B & S4).

To examine how contextual interactions among stimuli might impact information coding in V1 in an anisotropic manner, we first determined how well we could decode the identity (orientation and phase) of the target, alone or in each of the crowding conditions, from simultaneously recorded V1 population activity using linear discriminant analysis (Figure 2). All distractor stimuli impaired decoding performance, with radial-out crowding showing the largest performance decrease (Figure 2).

We next sought to understand how distractor location differentially influences information processing among laminar cortical circuit components. For our main analyses, we chose to focus on the broad-spiking populations, because these represent the primary output neurons of the column. For each subpopulation, we calculated the decoding performance for the target-only and crowding conditions (Figure 3; see Figure S3A for narrow-spiking populations). Most crowding stimuli impaired decoding performance compared to the target-only in most subpopulations (Figure 3 & S3A). In particular, the impairment of decoding performance was worse in the radial-out condition compared to the tangential and radial-in conditions among broad-spiking neurons in the

input and superficial layers, the two subpopulations that are key nodes in the feed-forward cortical information flow pathway (Figure 3, middle and top). Surprisingly, tangential crowding more strongly impaired decoding in the deep layers (Figure 3, bottom). Radial-out crowding also impaired decoding performance more than radial-in crowding in narrow-spiking neurons across all layers, although radial-out crowding had a similar impact compared to tangential crowding in these subpopulations (Figure S3A). Consistent with previous reports (*24*), we also found that more effective crowding stimuli (radial-out crowding) most strongly reduced spike-count correlations, and this result was strongest in the feed-forward pathway (Figure S3B-C).

Because distractor location has an anisotropic impact on the ability to decode target orientation from population activity, we investigated whether differential modulation in the tuning properties of V1 neurons could underlie these changes. We normalized the tuning curve for each single unit based on its preferred target orientation (see Methods) and plotted the average tuning curve of each subpopulation in response to the target only and in the crowding conditions (Figure 4A & S4A). Distractors broadened the tuning curves of V1 neurons in each of the subpopulations (Figure 4 & S4A). All subpopulations showed substantially reduced responses when distractors were presented alone (Figure S4C).

To quantify how distractor location modulated tuning, we first calculated the firing rates in response to preferred and orthogonal-to-preferred (orthogonal) target orientations. Crowding stimuli reduced firing rates in response to the preferred target orientation and increased the firing rates in response to the orthogonal target orientation (Figure 4B & S4B). This correspondingly resulted in a decrease in orientation selectivity

index (OSI) that was similar across crowding conditions (Figure S2C). Although OSI was similar across conditions and subpopulations, there were distinct differences in how flanker location modulated preferred and orthogonal firing rates. In broad-spiking neurons in both the input and superficial layers, radial-out flankers resulted in less suppression of firing to the preferred orientation, but more effectively facilitated firing in response to the orthogonal orientation (Figure 4B, middle and top). This pattern was also consistent among narrow-spiking neurons in the input layer (Figure S4B, top). These differences were not due to changes in average eye position across conditions (Figure S4D).

To further characterize these results and obtain mechanistic insights into these changes in tuning properties, we quantified the extent to which distractor location induced untuned additive facilitation or tuned divisive suppression (*23, 24*) of V1 tuning curves. We modeled each neuron's tuning curve in the target-only condition and then calculated the extent to which the responses to stimuli under each of the crowding conditions were best explained by additive and multiplicative shifts to the target-only tuning curve (Figure 5 & S5). Input and superficial layer broad-spiking neurons under radial-out crowding showed greater additive facilitation compared to tangential or radial-in crowding. (Figure 5A, middle and top). The radial-out condition also showed greater divisive suppression in broad-spiking neurons in both the input and superficial layers compared to the tangential and radial-in conditions (Figure 5B, top and middle). This effect was similar in narrow-spiking neurons in the input and superficial layers, with radial-out crowding showing more divisive suppression in both subpopulations compared to radial-in crowding and trending towards more suppression compared to tangential crowding (Figure S5B, top and middle).

We finally sought to understand how anisotropic integration could be explained in the context of normalization, a powerful explanatory framework for cortical computations (*41, 42*). We adapted the normalization model (*43*) by skewing the inhibitory kernel towards the fovea and introduced an additional additive kernel that was also skewed towards the fovea (Figure 6A, see Methods). For simplicity, visual space in the model is one-dimensional along the radial axis, and thus we chose to include only radial-in and radial-out crowding conditions. With these skewed kernels, orientation tuning curves for neurons with receptive fields at the target location were substantially broader under radial-out crowding than radial-in crowding or when the target was presented alone (Figure 6B). The population response of neurons with receptive fields at the target location was more strongly disrupted by the radial-out distractor compared to the radial-in distractor (Figure 6C). Moreover, the tuning curves predicted by the model in the different crowding conditions qualitatively resembled the population-averaged tuning curves for broad-spiking neurons in the input layer (Figure 6D).

The skewed normalization model suggests that stimuli should elicit stronger responses in neurons with receptive fields that are less eccentric compared to neurons with more eccentric receptive fields. This led us to predict that neurons with receptive fields at the target location should respond more to the radial-out distractor when presented alone (without the target stimulus) than to the radial-in distractor alone. Indeed, broad-spiking neurons in the input and superficial layers had higher firing rates when the distractor was presented at the radial-out location compared to the radial-in location (Figure 6E & S6), as did narrow-spiking neurons in the input layer (Figure 6E & S6). This analysis thus provides direct evidence of skewed kernels in visual cortex and confirms

our model prediction that a stimulus would exert a stronger influence on neurons with less eccentric receptive fields even when presented alone.

Taken together, these results show that radial-out crowding most effectively broadened tuning in broad-spiking neurons in the feed-forward pathway through untuned facilitation and tuned suppression. We propose this anisotropic interaction among stimuli could be explained by skewed additive and inhibitory interactions among neurons in V1.

DISCUSSION

Natural vision activates neurons not in isolation, but in the context of other stimuli. The extensive literature on contextual interactions in the visual cortex, particularly surround modulation (*44-52*), has significantly enriched our understanding of visual processing. However, a prevailing assumption in this literature has been the isotropic nature of the surrounding context. This is evident in the experimental design of contextual stimuli typically as annuli or as a circular constellation of flankers (*44, 45, 48, 53*). While several studies (*54-56*) did explore the spatial distribution of contextual interactions and their impact on neural responses, systematic geometrical arrangements of target and flanker objects with respect to the center of gaze were not investigated. Furthermore, it has been shown that intrinsic horizontal connections in V1 are anisotropic in a manner that could facilitate contour processing, enriching connections among neurons with orientation preferences and receptive fields that facilitate the detection of smooth contours (*57, 58*). But here too the spatial geometries alluded to above have not been investigated.

In contrast, perceptual asymmetries in vision have garnered considerable interest in the past several decades(*59-62*). In particular, the polar angle with respect to the center of gaze has been shown to be especially relevant to perceptual performance (see review

by (*63*)). Perceptual asymmetries are especially striking in the phenomenology of visual crowding wherein distractors impair target identification over a distinctive elongated zone in visual space. Cortical magnification results in radial-out distractors being represented closer to the target in cortical space compared to radial-in distractors, potentially explaining some of the anisotropy (*9, 10, 64*). However, it has been shown that considerations of cortical magnification alone are not sufficient to explain the marked elongation of the crowding zones along the radial axis defined by the center of gaze and the target stimulus (*8*).

Macaques experience crowding similar to humans, impairing their ability to discriminate the orientation of target stimuli (*22, 23*), and are thus a good model for studying the neural mechanisms of crowding. Experiments in both macaques and humans suggest that crowding can influence neural activity as early as V1 (*23, 65*), including a radial-tangential anisotropy in BOLD responses in V1 (*66*). The present study extends these findings by revealing the impact of distractor location on stimulus representation in the laminar microcircuit of the primary visual cortex and the neural mechanisms underlying these impacted representations.

Notably, the effects of radial-out crowding were more pronounced compared to tangential and radial-in crowding across various measures. These effects included the ability to decode target identity from simultaneously recorded populations, as well as from putative excitatory neurons in the input and superficial layers. Anisotropies were also evident in the modulation of tuning curves in these layers, with radial-out crowding producing stronger broadening of tuning curves through untuned additive facilitation and tuned divisive suppression. Additionally, radial-out distractors exhibited the most

substantial decrease in spike-count correlations in the input and superficial layers. While decreases in correlation are typically associated with increased information coding capacity, correlations are not necessarily information limiting, and decreased correlation can worsen the encoding capacity of a population (*67, 68*). These anisotropies likely contribute to the impaired perception of target stimuli induced by radial-out distractors. Importantly, the decreased ability to decode stimulus orientation from neural activity at the subpopulation level was not solely attributable to changes in spike-count correlations, as correlations were removed across all conditions for those analyses.

Surprisingly, we discovered that contextual interactions exhibit anisotropy even at the earliest stages of processing in V1, specifically within the input layer. This finding suggests a potential sub-cortical origin of the observed anisotropies (*69-73*). Additionally, we observed the presence of anisotropy in the superficial layer of V1, implying that these computations are partially inherited from the input layer. Broad-spiking neurons share electrophysiological characteristics with excitatory pyramidal neurons (*33, 35, 39*). Given that broad-spiking putative excitatory neurons in the superficial layer are likely projection neurons to downstream ventral visual areas (*25, 74-76*), our findings suggest that the anisotropic signaling is propagated along the feedforward pathway and could form the basis of the perceptual anisotropies underlying visual crowding.

In contrast, we did not find the same anisotropy in the deep layers of V1. This intriguing result suggests the emergence of novel contextual computations in the deep layers, indicating that tuning and response properties are not merely inherited from input and superficial layer projections to the deep layers. This is in agreement with previous findings that neurons in the deep layers can have differences in orientation tuning

compared to the superficial layers (*77, 78*) and that intrinsic (horizontal) connections in the deep layers are less extensive compared to the superficial layers (*79*). Moreover, as deep-layer broad-spiking putative excitatory neurons are the likely sources of feedback projections to subcortical areas, these feedback signals are likely not anisotropic. Despite the likely feedforward propagation of anisotropic signals, the absence of anisotropy in the feedback pathway suggests a mechanism of active cancellation in this important modulatory pathway.

The implications of our findings extend to the integration of information from outside the classical receptive field in the visual cortex. Orientation tuning properties and their modulation are determined by the balance of excitation and inhibition to cortical neurons (*80, 81*). Recurrent excitation (*82*) and lateral inhibition (*83*) are two key intra-cortical motifs that determine this balance. Cross-orientation suppression (*84*), a form of lateral inhibition likely plays an important role in shaping the cortical activity due to flanker-target interactions examined in this study. Such suppressive activity may operate in several ways according to orientation dependence and the strength of inhibitory connections and have been described in various models of cortical activity including those with attractor dynamics (*85, 86*), recurrence (*82*), balance (*87-89*), push-pull (*90, 91*) and normalization (*92-94*). Our results imply that distractor location differentially impacts the balance of excitation and inhibition in the laminar cortical circuit. Normalization, in particular, has been proposed as a canonical computation in the cortex (*42*) that explains a wide range of cortical phenomena including contrast response properties of visual neurons (*93, 95, 96*), multi-sensory integration (*97*), and multiple forms of attentional modulation (*43*) while remaining agnostic to the exact nature of the underlying biophysical

mechanisms referred to above. Our modeling and empirical results show that the fundamental assumption of symmetry in the spatial kernels of the normalization model must be broken to account for the anisotropic nature of contextual integration in the visual cortex. Future empirical and computational modeling studies of surround modulation should take this anisotropic and layer-specific integration into account.

In conclusion, this study provides compelling evidence that contextual interactions in the visual cortex exhibit anisotropy at the earliest stages of cortical processing of visual signals. Distractors broaden V1 orientation tuning curves in a spatially anisotropic manner. Radial-out distractors most effectively broaden tuning in the feedforward pathway through untuned facilitation and tuned suppression. These findings advance our understanding of the neural bases of visual crowding and offer mechanistic insights into the processing of contextual signals in the visual cortex.

AUTHOR CONTRIBUTIONS

MPM and ASN conceptualized the project. MPM collected the data, with assistance from SD and NVH. MPM analyzed the data. ASN supervised the project. MPM and ASN wrote the paper.

ACKNOWLEDGEMENTS

We would like to thank Steve Chang, Weikang Shi and Alec Sheffield for their helpful comments on the manuscript. This research was supported by NIH/NEI R01 EY032555, NARSAD Young Investigator Grant, Ziegler Foundation Grant, and Yale Orthwein Scholar Funds to ASN, NIH/NINDS training grants T32-NS007224 and T32-NS041228 to MPM, and by an NIH/NEI core grant for vision research P30 EY026878 to Yale University. We

would like to thank the veterinary and husbandry staff at Yale for excellent animal care.

FIGURE LEGENDS

Figure 1. Contextual interaction task and single-unit recordings.
(**A**) Task schematic. Stimuli were presented alone at the receptive field center (target only) or with a distractor at one of the four locations surrounding the target. The radial axis connects the target to the center of gaze, and the tangential axis is orthogonal to it, also passing through the target. The top schematic shows stimuli at all possible locations, while the bottom section shows the possible spatial configurations for the presentation of an individual stimulus array. (**B**) Data recorded from a single trial, including spikes (black vertical ticks) and local field potentials (black traces) collected from each channel on one of the two shanks of the laminar probe. Data is arranged vertically based on the spatial location of the recording channel. Cortical layers are indicated on the left (green=superficial, gray=input, pink=deep). Vertical bars indicate the time of stimulus onsets. (**C**) Example receptive field contours vertically stacked for each recording site along the depth of a shank on the laminar probe. (**D**) Example current source density (CSD) map showing the early current sink (red) indicative of the input layer. (**E**) Mean waveforms for all recorded single-units (blue=narrow-spiking, orange=broad-spiking). (**F**) Distribution of waveform durations (trough-to-peak time) for all recorded single-units across the two monkeys. Neurons with waveform durations less than 350µs were classified as narrow-spiking (blue), and neurons with waveform durations greater than 350µs were classified as broad-spiking (orange).

Figure 2. Distractor stimuli impair decoding performance in simultaneously recorded populations in an anisotropic manner.
Decoding performance from two example sessions in each monkey in the target-only condition and each of the three crowding conditions. Points in the upper section of each plot show the decoding performance for each of the 20 different cross-validations. The lower section for each session shows the bootstrapped estimation of the difference between decoding performance in each crowding condition compared to the target-only condition. Half-violin plots show the bootstrapped distribution of the difference, and black dots and bars represent the mean and 95% confidence intervals of the difference in decoding performance.

Figure 3. Radial-out crowding most strongly impairs decoding in the feed-forward pathway.
Decoding performance from broad-spiking neurons in each layer in the target-only condition and each of the three crowding conditions. Points in the upper section of each plot show the decoding performance for each of the 20 different cross-validations. The lower section for each layer shows the bootstrapped estimation of the difference between decoding performance in each crowding condition compared to the target-only condition. Half-violin plots show the bootstrapped distribution of the difference, and black dots and bars represent the mean and 95% confidence intervals of the difference in decoding performance.

Figure 4. Crowding stimuli modulate the tuning curves of V1 neurons.
(**A**) Normalized tuning curves for broad-spiking neurons in each layer in the target-only and crowding conditions. Tuning curves are aligned with the preferred orientation at 0 degrees and duplicated to fill the circle. Tuning curves were normalized by the maximum firing rate in the target-only condition. Lines and shading represent mean +/- s.e.m. (black=target only, pink=tangential crowding, green=radial-in crowding, purple=radial-out crowding). (**B**) Difference in firing rate in response to preferred (dark brown) and orthogonal (light tan) stimuli under each crowding condition across layers. Colored half-violin plots show the bootstrapped estimation of the paired mean difference in firing rate for a given subpopulation, crowding condition, and stimulus orientation. Black dots and lines represent the mean and 95% confidence interval of the estimated difference.

Figure 5. Radial-out crowding causes stronger additive facilitation and divisive suppression of tuning curves.
(**A**) Difference in the modeled (see Methods) untuned additive facilitation of tuning curves of broad-spiking neurons caused by each of the crowding conditions. Gray half-violin plots show the bootstrapped estimation of the paired mean difference in the modeled additive component for a given subpopulation and pair of crowding conditions. Black dots and lines represent the mean and 95% confidence interval of the estimated difference. (**B**) Same as (**A**) but for the multiplicative component, reflecting tuned divisive suppression.

Figure 6. Normalization model with spatially skewed additive and divisive components explains crowding anisotropy.
(**A**) Excitatory (blue), inhibitory (red), and additive (cyan) kernels used in the normalization model. The additive and inhibitory kernels are skewed by doubling their standard deviation in the foveal direction and scaling both sides to maintain a smooth curve. (**B**) Modeled tuning curves in the target only (black), radial-in crowding (green), and radial-out crowding (purple). (**C**) Modeled population response in the three conditions: target only (left), radial-in crowding (middle), and radial-out crowding (right). (**D**) Comparison of population-averaged tuning curves from input-layer broad-spiking neurons (top, same as Figure 4A) and modeled tuning curves (bottom). (**E**) Difference in firing rate for each of the six subpopulations when a flanking stimulus was presented alone in the radial-out position compared to the radial-in position without the target present. Black dots and lines represent the mean and 95% confidence interval of the estimated difference.

Figure S1. Laminar recordings in V1.
(**A**) Section perspective schematic of the artificial dura recording chamber and laminar probe. (**B**) Photo of the artificial dura chamber in one monkey.

Figure S2. Peri-stimulus time histograms, tuning curves of single units, and orientation selectivity index under crowding.
(**A**) Peri-stimulus time histogram (PSTH) of subpopulations in each condition following the onset of the preferred stimulus. The preferred orientation was calculated separately for each single unit. Spikes were counted in 30ms bins shifted by 5ms. Error bars show mean+/- s.e.m. (**B**) Example single unit tuning curves in the target-only condition. Single units were selected from multiple different recording sessions. (**C**) Difference in orientation selectivity index (OSI) in each of the crowding conditions compared to the target-only condition. Colored half-violin plots show the bootstrapped estimation of the mean difference in OSI for a given subpopulation and crowding condition. Black dots and lines represent the mean and 95% confidence interval of the estimated difference.

Figure S3. Decoding performance in narrow-spiking neurons and spike-count correlations
(**A**) Decoding performance from narrow-spiking neurons in each layer in the target-only condition and each of the three crowding conditions. Points in the upper section of each plot show the decoding performance for each of the 20 different cross-validations. The lower section for each layer shows the bootstrapped estimation of the difference between decoding performance in each crowding condition compared to the target-only condition. Half-violin plots show the bootstrapped distribution of the difference, and black dots and bars represent the mean and 95% confidence intervals of the difference in decoding performance. (**B**) Spike-count correlations from pairs of simultaneously recorded neurons in each subpopulation in the target-only condition and each of the three crowding conditions. In the top panels, error bars represent mean +/- 95% confidence intervals of the spike-count correlation in each condition. In the bottom panels, black dots and lines represent the mean and 95% confidence interval of the estimated difference from the target-only condition, and colored half-violin plots show the bootstrapped estimation of the mean difference in spike-count correlation for a given subpopulation and crowding condition. (**C**) Spike-count correlations for each pair of single units in each subpopulation. Each point represents the spike-count correlations of one pair of simultaneously recorded neurons in the same layer and cell class and each condition.

Figure S4. Tuning curves of narrow-spiking neurons, responses to flanker only, and eye position data.
(**A**) Normalized tuning curves for narrow-spiking neurons in each layer in the target-only and crowding conditions. Tuning curves are aligned with the preferred orientation at 0 degrees and duplicated to fill the circle. Tuning curves were normalized by the maximum firing rate in the target-only condition. Lines and shading represent mean +/- s.e.m. (black=target only, pink=tangential crowding, green=radial-in crowding, purple=radial-out

crowding). (**B**) Difference in firing rate in response to preferred (dark brown) and orthogonal (light tan) stimuli under each crowding condition among narrow spiking neurons in each layer. Colored half-violin plots show the bootstrapped estimation of the paired mean difference in firing rate for a given subpopulation, crowding condition, and stimulus orientation. Black dots and lines represent the mean and 95% confidence interval of the estimated difference. (**C**) Normalized tuning curves for each subpopulation in the target-only and distractor-only conditions. Tuning curves are aligned with the preferred orientation at 0 degrees and duplicated to fill the circle. Tuning curves were normalized by the maximum firing rate in the target-only condition. The distractor-only condition is plotted relative to the orientation of the distractor and combines data from all four distractor positions. Lines and shading represent mean +/- s.e.m. (black=target only, gold=distractor only). (**D**) Mean eye position during the four conditions in each recording session. Each session has five points plotted (target only, radial-in crowding, radial-out crowding, and tangential clockwise crowding as dots, tangential counter-clockwise as stars). Above and to the right are marginal distributions of the median x and y positions for each of the sessions in each condition (tangential counter-clockwise plotted as a dashed line). To account for different target positioning across sessions, all data are rotated such that the target stimulus is to the right.

Figure S5. Single-unit tuning model parameters in different crowding conditions
(**A**) Difference in the modeled (see Methods) untuned additive facilitation (left) and multiplicative suppression (right) caused by each of the crowding conditions among narrow-spiking units. Gray half-violin plots show the bootstrapped estimation of the paired mean difference in the modeled additive component for a given subpopulation and pair of crowding conditions. Black dots and lines represent the mean and 95% confidence interval of the estimated difference. (**B**) Related to Figure 5A and S5A left. Value of the fitted additive parameter for each neuron in each crowding condition. Each line represents the additive parameter for a single unit in across the two crowding conditions indicated at the bottom. (**C**) Related to Figure 5B and S5A right. Same as (**B**) but for the multiplicative component.

Figure S6. Single-unit firing rates in response to flanker alone
The average firing rate response of each neuron to stimuli in the radial-in or radial-out crowding position is shown on the left side of the plot for each subpopulation. On the right, gray half-violin plots show the bootstrapped estimation of the paired mean difference in firing rate for a given subpopulation and pair of crowding conditions. Black dots and lines represent the mean and 95% confidence interval of the estimated difference. Estimation statistics plots are the same as those in Figure 6E but scaled based on the raw firing rates shown here so that axes on the left and right are identical.

MATERIALS & METHODS

Data Collection

Surgical procedures

Surgical procedures were similar to those described previously (*29, 30, 98*). We placed low-profile titanium recording chambers in two rhesus macaques so that the chambers allowed access to area V1 (right hemisphere in monkey D, left hemisphere in monkey M). Chambers were targeted based on sulcus reconstructions created using preoperative structural MRI. After chamber implantation, we removed the native dura mater and replaced it with a transparent silicone artificial dura (AD). The AD allowed for the visualization of cortical sites in V1 for probe targeting. All procedures were approved by the Yale University Institutional Animal Care and Use Committee and conformed to NIH guidelines.

Electrophysiology

Prior to a series of recordings, we electroplated (nanoZ, White Matter LLC) 64-channel electrode arrays ("laminar probes," NeuroNexus Technologies, Inc., 2 shanks, 32 channels/shank, 70µm spacing between sites, 200µm between shanks) with PEDOT (poly(3,4-ethylene dioxythiophene)). At the beginning of each recording session, we inserted a laminar probe in V1. Laminar probes were attached to a titanium mounting stage that was screwed into the chamber. We positioned the laminar probes using an electronic micromanipulator (Narishige Inc.) and ensured that the probes were orthogonal to the surface of the cortex by visual inspection through a surgical microscope (Leica Microsystems). To position the probe within the brain, we first penetrated the AD, arachnoid, and pia by moving the probe downward at a high speed (>100µm/s). After the tip of the probe entered the cortex, we inserted the remainder of the probe at a slow speed (2µm/s). Once the entire probe was in the brain, we slowly (2µm/s) relieved the pressure

on the brain by retracting the probe upward, relieving pressure on the brain but not moving the probe relative to the cortex.

Electrical signals from the laminar probe were collected at 30kHz and digitized on a 64-channel digital headstage and sent to the recording system (RHD Recording System, Intan Technologies). Action potential waveforms were extracted offline using Kilosort2 (*99, 100*) and manually sorted into single and multi-unit clusters (Phy; *99, 100*). Multi-unit clusters were excluded from further analysis. Single-unit clusters were classified based on their trough-to-peak waveform duration into broad- and narrow-spiking units (*29, 31*). Neurons with waveform durations less than 350µs were classified as narrow-spiking while those with waveform durations longer than 350µs were classified as broad-spiking. Clusters with peaks preceding the trough were identified as axonal spikes and excluded. Recordings were collected over the course of 22 sessions (9 in monkey D, 13 in monkey M) with hundreds of single units recorded in each subject (384 in monkey D, 521 in monkey M).

Behavioral Control and Eye Tracking

We controlled behavioral experiments using NIMH MonkeyLogic (*101*). Eye position and pupil diameter were sampled at 120Hz (ETL-200, ISCAN Inc.) and sent to the behavioral control system. Stimuli were presented on a monitor positioned 57cm from the monkey with a 60Hz refresh rate. Trials were aborted if the eye position deviated more than 1.2-1.5 degrees of visual angle (dva; 1.2 for monkey D, 1.5 for monkey M) from the central fixation point.

Receptive Field Mapping

We mapped RFs of the column by presenting Gabor patch stimuli (2-4 cycles/degree,

0.25-1 degree Gaussian half-width, 100% luminance contrast) on a square grid spanning the lower visual quadrant of interest (left in monkey D, right in monkey M) while the monkey maintained fixation on the center of the screen. Grid spacing parameters were optimized each session and ranged from 0.25-1 dva. A stimulus was presented at a random location and orientation on the grid during each frame. We calculated the LFP power for each recording channel 40-200ms after stimulus presentation in each location. The LFP power at each location was smoothed using a Gaussian kernel (sigma = 0.75 dva), and the peak location averaged across all recording sites was defined as the RF center. Spatial RF maps for each channel were plotted as stacked contours for each shank for visualization. The RF center was determined from the aggregate RF across all shanks and channels.

Current Source Density Mapping

We used CSD mapping (*40*) to identify laminar boundaries in our recordings. While monkeys maintained fixation on the screen, 100% luminance contrast white annular stimuli were flashed for 32ms, positioned at the center of the RF. The CSD was calculated as the second spatial derivative of the LFP following stimulus onset. CSD traces were spatially smoothed using a Gaussian kernel (sigma = 140µm). The input layer was identified by the boundaries of the early current sink characterizing feed-forward input into layer IV. Channels above and below this sink were classified as superficial and deep respectively.

Anisotropic Crowding Task

While monkeys maintained fixation, stimulus arrays were flashed on the screen for 100ms and off the screen for 200ms. The target location was at the center of the aggregate RF

of all channels. The arrays consisted of a target stimulus in the RF center either in isolation (target only) or together with a distractor stimulus (crowding). There were four different conditions (target only, tangential crowding, radial-in crowding, and radial-out crowding) of stimulus arrays presented during a trial. This was repeated 4-6 times during each trial depending on the monkey's ability to hold fixation. The stimulus conditions were randomly interleaved from flash to flash. The center of the target stimulus was aligned with the center of the average of the RFs of each recording site. The four distractor locations were positioned on the radial or tangential axes. The radial axis was defined as the axis connecting the target (and RF) center and the fixation point at the center of the monitor. The tangential axis was defined as the line orthogonal to the radial axis and passing through the target center. The tangential crowding condition occurred when the target was presented along with a distractor stimulus on the tangential axis, either in the clockwise or counterclockwise direction. The radial-in crowding condition occurred when the target was presented along with a distractor stimulus on the radial axis and between the target center and the fixation point. The radial-out condition was similar to the radial-in condition, except the distractor stimulus was placed on the radial axis further from the fixation point than the target. Target-distractor spacing was identical across stimulus conditions.

The target-only condition was presented on 10% of flashes. On 80% of flashes, crowding stimuli were presented. In the crowding condition, the distractor stimulus was positioned at a tangential, radial-in, or radial-out location with equal probability. If the distractor was presented tangential to the target, it was positioned clockwise or counterclockwise to the target with equal probability. In the remaining 10% of trials, a

stimulus was presented exclusively at one of the four distractor locations. Target stimuli were sine Gabor patches (25% luminance contrast, 3.5 cycles/degree, 0.5-1.0 degree Gaussian half-width) presented at 6 evenly spaced orientations and 2 opposing phases. Flanking stimuli were presented at 100% luminance contrast but were otherwise identical to the target stimuli. There was a 0.1-0.2 degree gap between the edges of the target and flanking stimuli (edge defined as 2 standard deviations from the center of the Gaussian). In the crowding condition, distractors were presented at the same orientation as the target or orthogonal to the target with equal probability. In this study, we focused exclusively on the condition in which the distractor was orthogonal to the target. When distractors were presented alone, they were shown with the same orientation distribution as the targets.

Data Analysis

Wherever possible, we analyzed our data using the estimation statistics framework (*102, 103*) and show bootstrapped estimations of differences between conditions rather than relying on null-hypothesis testing. The estimation statistics framework provides a principled way to measure effect sizes coupled with estimates of uncertainty, yielding interval estimates of uncertainty.

Tuning Curve Visualization

To visualize the modulation of tuning curves of each subpopulation by distractor stimuli, we calculated the number of spikes for each neuron 0-300ms following stimulus onset in each orientation and condition, collapsing across phases, and subtracted the baseline firing rate (0-100ms before stimulus onset). For each neuron, we identified the orientation with the highest firing rate in the target-only condition as the preferred orientation and

shifted the tuning curves to set this orientation to 0 degrees in each condition. We then normalized the turning curves by dividing each neuron's response to each orientation and condition by the firing rate for the preferred target-only orientation. For visualization, the tuning curve was duplicated and rotated 180 degrees to completely fit around a circle. We excluded neurons that did not respond in the target-only condition. To visualize the tuning curves of individual single units, we followed the same procedure but did not average across phases, instead plotting the response to each phase as the opposite orientation. Additionally, single-unit tuning curves were not rotated based on the preferred orientation.

Preferred and Orthogonal Firing Rate and OSI

OSI was calculated using the following equation:

$$OSI = \frac{FR_{pref} - FR_{orth}}{FR_{pref} + FR_{orth}}$$

Where FR_{pref} is the firing rate in response to the preferred orientation and FR_{orth} is the firing rate in response to the stimulus orthogonal to the preferred orientation. Firing rates were calculated 0-300ms following stimulus onset. The preferred orientation was identified as the orientation with the highest firing rate. FR_{pref}, FR_{orth} , and OSI were compared between the target-only condition and the crowding conditions by calculating the bootstrapped estimation of the mean difference.

Modeling Tuning Curve Modulation

We investigated the components of single-unit tuning curve modulation using a previously published approach to identify additive and multiplicative changes to tuning curves (*24*). Briefly, we fit a Poisson model based on spike counts from 0-300ms after stimulus onset in the target-only condition for each orientation. We then calculated the untuned additive

and tuned multiplicative modulation of the fitted target-only tuning curve that would best account for the observed spike counts independently for each crowding condition (*24*). We then compared the additive and multiplicative parameters for each neuron across conditions by calculating a bootstrapped estimation of the paired mean difference of the components.

Decoding Analysis

We trained a decoder using linear discriminant analysis (LDA) to determine the identity (orientation and phase) of a target stimulus from simultaneously recorded single-unit activity. Spike counts were calculated from 0-300ms following stimulus onset. The decoder performance was determined using 20-fold cross-validation. The decoder was trained on stimuli presented in the target-only condition and tested on neural responses in each of the crowding conditions. This procedure was repeated for each recording session. Performance in the tangential crowding condition was calculated separately for the two tangential locations and averaged.

To calculate decoding performance at the subpopulation level, we first generated a database of pseudo-population activity for each neuron in every combination of conditions and target orientations. Spike counts were calculated from 0-300ms following stimulus onset. To train the decoder for each subpopulation, we generated pseudo-population activity by randomly drawing samples from this database, independently for each neuron. We trained separate decoders for each subpopulation, training and testing on responses from every neuron in each cell class and layer across all recording sessions. Decoders were trained by sampling from data in the target-only condition. 20% of each neuron's responses to each orientation were held out (the subset was

independent for each neuron) for cross-validation. This procedure was repeated 20 times with a different random subset of responses used for cross-validation in the target-only condition. The decoding performance on this 20% of left-out data was considered the decoding performance in the target-only condition. We then tested each decoder on pseudo-population activity generated from responses in the crowding conditions.

Peri-stimulus time histograms (PSTH)

PSTHs were generated based on spike counts in 30ms bins shifted by 5ms. PSTHs are shown only for the preferred orientation as defined previously. The PSTH for each neuron was calculated separately for each condition, and the average PSTH for each subpopulation was plotted in Figure S2A. All times are relative to stimulus onset.

Spike-count correlations

Spike-count correlations were calculated for each pair of simultaneously recorded neurons in the same layer and broad- or narrow-spiking cell class. Spike counts were extracted from 100-300ms after stimulus onset and normalized by Z-score for each stimulus orientation and condition. For each condition, the spike-count correlation was calculated separately for each orientation from the normalized spike counts and was then averaged across orientations. Thus, each pair of neurons had a single spike-count correlation number for each stimulus condition.

Eye-position analysis

In each session, we calculated the monkey's average eye position in the time period from 50ms before to 150ms after each stimulus presentation. We then averaged these positions for each stimulus category: target only, radial-in crowding, radial-out crowding, and tangential (clockwise and countreclockwise) crowding within each session to obtain

one value per condition and session. To compare across all sessions, we rotated the mean eye position values based on the location of the target stimulus so that the target was always to the right in Figure S4D.

Normalization model

Our model was based on the normalization model presented by Reynolds and Heeger (*43, their Figure 1*). We excluded any attentional effects by making the attentional field uniform across both space and orientation. To make our kernels asymmetrical, we doubled the standard deviation of the Gaussian for the inhibitory and additive kernels on the foveal side and scaled both sides to maintain a smooth contour (Figure 6A). The Gaussians underlying the inhibitory and additive kernels were identical in shape.

The responses of neurons were calculated similarly to the previously described model (*43*) using the same notation:

$$\mathrm{R}(\mathrm{x},\theta) = |\mathrm{A}(\mathrm{x},\theta) + \mathrm{E}(\mathrm{x},\theta)/[\mathrm{S}(\mathrm{x},\theta) + \sigma]|_{\mathrm{T}}$$

Where R is the response of a neuron, x represents its receptive field center, and θ its orientation preference. E is the excitatory drive, S is the suppressive drive, σ is a constant that determines the contrast gain, and T is the rectification threshold. A is the additive drive defined as:

$$\mathrm{A}(\mathrm{x},\theta) = \mathrm{a}(\mathrm{x},\theta) * \mathrm{E}(\mathrm{x},\theta)$$

Where $\mathrm{a}(\mathrm{x},\theta)$ is the asymmetrical additive kernel and * is convolution.

Additional model parameters are presented below:

Parameter	**Value**
Additive kernel spatial standard deviation	2 dva (towards periphery) 4 dva (towards fovea)
Inhibitory kernel spatial standard deviation	2 dva (towards periphery) 4 dva (towards fovea)
Excitatory kernel spatial standard deviation	0.5 dva

Additive kernel orientation standard deviation	360 degrees
Inhibitory kernel orientation standard deviation	360 degrees
Excitatory kernel orientation standard deviation	30 degrees
Stimulus size	1 dva
Target-flanker spacing	5 dva

Flanker-only firing responses

We calculated the firing rate of neurons from spikes occurring 0-300ms after flanker only stimulus onset. Firing rates were calculated for each stimulus position regardless of orientation. Neurons were split by cell class and layer and their firing rate was compared across stimulus locations.

REFERENCES

1. H. Bouma, Interaction Effects in Parafoveal Letter Recognition. *Nature* **226**, 177-178 (1970).
2. D. V. Meegan, S. P. Tipper, Reaching into cluttered visual environments: spatial and temporal influences of distracting objects. *Q J Exp Psychol A* **51**, 225-249 (1998).
3. D. Whitney, D. M. Levi, Visual crowding: a fundamental limit on conscious perception and object recognition. *Trends in Cognitive Sciences* **15**, 160-168 (2011).
4. A. Toet, D. M. Levi, The two-dimensional shape of spatial interaction zones in the parafovea. *Vision Res* **32**, 1349-1357 (1992).
5. Y. Petrov, A. V. Popple, S. P. McKee, Crowding and surround suppression: Not to be confused. *Journal of Vision* **7**, 12-12 (2007).
6. M. C. Flom, G. G. Heath, E. Takahashi, CONTOUR INTERACTION AND VISUAL RESOLUTION: CONTRALATERAL EFFECTS. *Science* **142**, 979-980 (1963).
7. S. P. Tripathy, D. M. Levi, Long-range dichoptic interactions in the human visual cortex in the region corresponding to the blind spot. *Vision Res* **34**, 1127-1138 (1994).
8. A. S. Nandy, B. S. Tjan, Saccade-confounded image statistics explain visual crowding. *Nature Neuroscience* **15**, 463-469 (2012).
9. D. G. Pelli, Crowding: a cortical constraint on object recognition. *Curr Opin Neurobiol* **18**, 445-451 (2008).
10. B. C. Motter, D. A. Simoni, The roles of cortical image separation and size in active visual search performance. *Journal of Vision* **7**, 6-6 (2007).

11. Y. Petrov, A. V. Popple, Crowding is directed to the fovea and preserves only feature contrast. *Journal of Vision* **7**, 8-8 (2007).
12. R. van den Berg, J. B. T. M. Roerdink, F. W. Cornelissen, A Neurophysiologically Plausible Population Code Model for Feature Integration Explains Visual Crowding. *PLOS Computational Biology* **6**, e1000646 (2010).
13. D. M. Levi, T. Carney, Crowding in peripheral vision: why bigger is better. *Curr Biol* **19**, 1988-1993 (2009).
14. J. Freeman, E. P. Simoncelli, Metamers of the ventral stream. *Nat Neurosci* **14**, 1195-1201 (2011).
15. D. M. Levi, Crowding—An essential bottleneck for object recognition: A mini-review. *Vision Research* **48**, 635-654 (2008).
16. L. Parkes, J. Lund, A. Angelucci, J. A. Solomon, M. Morgan, Compulsory averaging of crowded orientation signals in human vision. *Nature Neuroscience* **4**, 739-744 (2001).
17. J. A. Greenwood, P. J. Bex, S. C. Dakin, Positional averaging explains crowding with letter-like stimuli. *Proceedings of the National Academy of Sciences* **106**, 13130-13135 (2009).
18. E. F. Ester, E. Zilber, J. T. Serences, Substitution and pooling in visual crowding induced by similar and dissimilar distractors. *J Vis* **15**, 15.11.14 (2015).
19. B. Balas, L. Nakano, R. Rosenholtz, A summary-statistic representation in peripheral vision explains visual crowding. *Journal of Vision* **9**, 13-13 (2009).
20. M. Manassi, D. Whitney, Multi-level Crowding and the Paradox of Object Recognition in Clutter. *Curr Biol* **28**, R127-r133 (2018).
21. D. G. Pelli, K. A. Tillman, The uncrowded window of object recognition. *Nat Neurosci* **11**, 1129-1135 (2008).
22. E. A. Crowder, C. R. Olson, Macaque monkeys experience visual crowding. *J Vis* **15**, 14 (2015).
23. C. A. Henry, A. Kohn, Spatial contextual effects in primary visual cortex limit feature representation under crowding. *Nature Communications* **11**, 1687 (2020).
24. C. A. Henry, A. Kohn, Feature representation under crowding in macaque V1 and V4 neuronal populations. *Current Biology* **32**, 5126-5137.e5123 (2022).
25. R. J. Douglas, K. A. C. Martin, NEURONAL CIRCUITS OF THE NEOCORTEX. *Annual Review of Neuroscience* **27**, 419-451 (2004).
26. B. Tasic *et al.*, Shared and distinct transcriptomic cell types across neocortical areas. *Nature* **563**, 72-78 (2018).
27. H. Zeng, J. R. Sanes, Neuronal cell-type classification: challenges, opportunities and the path forward. *Nature Reviews Neuroscience* **18**, 530-546 (2017).
28. M. Migliore, G. M. Shepherd, An integrated approach to classifying neuronal phenotypes. *Nature Reviews Neuroscience* **6**, 810-818 (2005).
29. A. S. Nandy, J. J. Nassi, J. H. Reynolds, Laminar Organization of Attentional Modulation in Macaque Visual Area V4. *Neuron* **93**, 235-246 (2017).
30. J. J. Nassi, M. C. Avery, A. H. Cetin, A. W. Roe, J. H. Reynolds, Optogenetic Activation of Normalization in Alert Macaque Visual Cortex. *Neuron* **86**, 1504-1517 (2015).

31. J. F. Mitchell, K. A. Sundberg, J. H. Reynolds, Differential attention-dependent response modulation across cell classes in macaque visual area V4. *Neuron* **55**, 131-141 (2007).
32. B. W. Connors, M. J. Gutnick, Intrinsic firing patterns of diverse neocortical neurons. *Trends Neurosci* **13**, 99-104 (1990).
33. D. A. McCormick, B. W. Connors, J. W. Lighthall, D. A. Prince, Comparative electrophysiology of pyramidal and sparsely spiny stellate neurons of the neocortex. *J Neurophysiol* **54**, 782-806 (1985).
34. Y. Kawaguchi, Groupings of nonpyramidal and pyramidal cells with specific physiological and morphological characteristics in rat frontal cortex. *Journal of Neurophysiology* **69**, 416-431 (1993).
35. L. G. Nowak, R. Azouz, M. V. Sanchez-Vives, C. M. Gray, D. A. McCormick, Electrophysiological classes of cat primary visual cortical neurons in vivo as revealed by quantitative analyses. *J Neurophysiol* **89**, 1541-1566 (2003).
36. D. Contreras, L. Palmer, Response to contrast of electrophysiologically defined cell classes in primary visual cortex. *The Journal of neuroscience : the official journal of the Society for Neuroscience* **23**, 6936-6945 (2003).
37. R. C. Foehring, N. M. Lorenzon, P. Herron, C. J. Wilson, Correlation of physiologically and morphologically identified neuronal types in human association cortex in vitro. *J Neurophysiol* **66**, 1825-1837 (1991).
38. N. V. Povysheva *et al.*, Properties of excitatory synaptic responses in fast-spiking interneurons and pyramidal cells from monkey and rat prefrontal cortex. *Cerebral cortex (New York, N.Y. : 1991)* **16**, 541-552 (2006).
39. A. Hasenstaub *et al.*, Inhibitory postsynaptic potentials carry synchronized frequency information in active cortical networks. *Neuron* **47**, 423-435 (2005).
40. U. Mitzdorf, Current source-density method and application in cat cerebral cortex: investigation of evoked potentials and EEG phenomena. *Physiol Rev* **65**, 37-100 (1985).
41. D. J. Heeger, E. P. Simoncelli, J. A. Movshon, Computational models of cortical visual processing. *Proceedings of the National Academy of Sciences* **93**, 623-627 (1996).
42. M. Carandini, D. J. Heeger, Normalization as a canonical neural computation. *Nature Reviews Neuroscience* **13**, 51-62 (2012).
43. J. H. Reynolds, D. J. Heeger, The Normalization Model of Attention. *Neuron* **61**, 168-185 (2009).
44. A. Angelucci *et al.*, Circuits and Mechanisms for Surround Modulation in Visual Cortex. *Annu Rev Neurosci* **40**, 425-451 (2017).
45. J. R. Cavanaugh, W. Bair, J. A. Movshon, Nature and interaction of signals from the receptive field center and surround in macaque V1 neurons. *J Neurophysiol* **88**, 2530-2546 (2002).
46. D. H. Hubel, T. N. Wiesel, RECEPTIVE FIELDS AND FUNCTIONAL ARCHITECTURE IN TWO NONSTRIATE VISUAL AREAS (18 AND 19) OF THE CAT. *J Neurophysiol* **28**, 229-289 (1965).
47. C. Blakemore, E. A. Tobin, Lateral inhibition between orientation detectors in the cat's visual cortex. *Experimental brain research* **15**, 439-440 (1972).

48. L. Maffei, A. Fiorentini, The unresponsive regions of visual cortical receptive fields. *Vision Research* **16**, 1131-IN1135 (1976).
49. C. D. Gilbert, Laminar differences in receptive field properties of cells in cat primary visual cortex. *J Physiol* **268**, 391-421 (1977).
50. J. I. Nelson, B. J. Frost, Orientation-selective inhibition from beyond the classic visual receptive field. *Brain Res* **139**, 359-365 (1978).
51. M. P. Sceniak, M. J. Hawken, R. Shapley, Visual spatial characterization of macaque V1 neurons. *J Neurophysiol* **85**, 1873-1887 (2001).
52. G. Van den Bergh, B. Zhang, L. Arckens, Y. M. Chino, Receptive-field properties of V1 and V2 neurons in mice and macaque monkeys. *The Journal of comparative neurology* **518**, 2051-2070 (2010).
53. S. Shushruth, J. M. Ichida, J. B. Levitt, A. Angelucci, Comparison of Spatial Summation Properties of Neurons in Macaque V1 and V2. *Journal of Neurophysiology* **102**, 2069-2083 (2009).
54. M. K. Kapadia, M. Ito, C. D. Gilbert, G. Westheimer, Improvement in visual sensitivity by changes in local context: parallel studies in human observers and in V1 of alert monkeys. *Neuron* **15**, 843-856 (1995).
55. M. K. Kapadia, G. Westheimer, C. D. Gilbert, Dynamics of spatial summation in primary visual cortex of alert monkeys. *Proc Natl Acad Sci U S A* **96**, 12073-12078 (1999).
56. M. K. Kapadia, G. Westheimer, C. D. Gilbert, Spatial distribution of contextual interactions in primary visual cortex and in visual perception. *J Neurophysiol* **84**, 2048-2062 (2000).
57. W. H. Bosking, Y. Zhang, B. Schofield, D. Fitzpatrick, Orientation selectivity and the arrangement of horizontal connections in tree shrew striate cortex. *The Journal of neuroscience : the official journal of the Society for Neuroscience* **17**, 2112-2127 (1997).
58. K. E. Schmidt, R. Goebel, S. Löwel, W. Singer, The Perceptual Grouping Criterion of Colinearity is Reflected by Anisotropies of Connections in the Primary Visual Cortex. *European Journal of Neuroscience* **9**, 1083-1089 (1997).
59. F. W. Campbell, J. J. Kulikowski, J. Levinson, The effect of orientation on the visual resolution of gratings. *J Physiol* **187**, 427-436 (1966).
60. J. A. Bauer, Jr., D. A. Owens, J. Thomas, R. Held, Monkeys show an oblique effect. *Perception* **8**, 247-253 (1979).
61. G. Westheimer, The distribution of preferred orientations in the peripheral visual field. *Vision Res* **43**, 53-57 (2003).
62. L. Liang, Y. Zhou, M. Zhang, Y. Pan, Revealing the Radial Effect on Orientation Discrimination by Manual Reaction Time. *Front Neurosci* **11**, 638 (2017).
63. M. M. Himmelberg, J. Winawer, M. Carrasco, Polar angle asymmetries in visual perception and neural architecture. *Trends Neurosci* **46**, 445-458 (2023).
64. J. Rovamo, V. Virsu, Isotropy of cortical magnification and topography of striate cortex. *Vision Res* **24**, 283-286 (1984).
65. R. Millin, A. C. Arman, S. T. L. Chung, B. S. Tjan, Visual Crowding in V1. *Cerebral Cortex* **24**, 3107-3115 (2013).
66. M. Kwon, P. Bao, R. Millin, B. S. Tjan, Radial-tangential anisotropy of crowding in the early visual areas. *J Neurophysiol* **112**, 2413-2422 (2014).

67. B. B. Averbeck, P. E. Latham, A. Pouget, Neural correlations, population coding and computation. *Nature Reviews Neuroscience* **7**, 358-366 (2006).
68. R. Moreno-Bote *et al.*, Information-limiting correlations. *Nat Neurosci* **17**, 1410-1417 (2014).
69. W. R. Levick, L. N. Thibos, Analysis of orientation bias in cat retina. *J Physiol* **329**, 243-261 (1982).
70. A. G. Leventhal, J. D. Schall, Structural basis of orientation sensitivity of cat retinal ganglion cells. *The Journal of comparative neurology* **220**, 465-475 (1983).
71. J. D. Schall, V. H. Perry, A. G. Leventhal, Retinal ganglion cell dendritic fields in old-world monkeys are oriented radially. *Brain Res* **368**, 18-23 (1986).
72. R. W. Rodieck, K. F. Binmoeller, J. Dineen, Parasol and midget ganglion cells of the human retina. *The Journal of comparative neurology* **233**, 115-132 (1985).
73. E. L. Smith, 3rd, Y. M. Chino, W. H. Ridder, 3rd, K. Kitagawa, A. Langston, Orientation bias of neurons in the lateral geniculate nucleus of macaque monkeys. *Vis Neurosci* **5**, 525-545 (1990).
74. V. B. Mountcastle, The columnar organization of the neocortex. *Brain* **120 (Pt 4)**, 701-722 (1997).
75. R. Gattass, A. Sousa, C. Gross, Visuotopic organization and extent of V3 and V4 of the macaque. *Journal of neuroscience* **8**, 1831-1845 (1988).
76. K. D. Harris, T. D. Mrsic-Flogel, Cortical connectivity and sensory coding. *Nature* **503**, 51-58 (2013).
77. R. Bauer, B. M. Dow, R. G. Vautin, Laminar distribution of preferred orientations in foveal striate cortex of the monkey. *Experimental brain research* **41**, 54-60 (1980).
78. R. Bauer, B. M. Dow, A. Z. Snyder, R. Vautin, Orientation shift between upper and lower layers in monkey visual cortex. *Experimental brain research* **50**, 133-145 (1983).
79. K. S. Rockland, J. S. Lund, Intrinsic laminar lattice connections in primate visual cortex. *The Journal of comparative neurology* **216**, 303-318 (1983).
80. N. J. Priebe, Mechanisms of Orientation Selectivity in the Primary Visual Cortex. *Annu Rev Vis Sci* **2**, 85-107 (2016).
81. K. A. Ferguson, J. A. Cardin, Mechanisms underlying gain modulation in the cortex. *Nature reviews. Neuroscience* **21**, 80-92 (2020).
82. R. J. Douglas, C. Koch, M. Mahowald, K. A. Martin, H. H. Suarez, Recurrent excitation in neocortical circuits. *Science* **269**, 981-985 (1995).
83. H. K. Hartline. (1949).
84. T. C. Freeman, S. Durand, D. C. Kiper, M. Carandini, Suppression without inhibition in visual cortex. *Neuron* **35**, 759-771 (2002).
85. R. Ben-Yishai, R. L. Bar-Or, H. Sompolinsky, Theory of orientation tuning in visual cortex. *Proc Natl Acad Sci U S A* **92**, 3844-3848 (1995).
86. D. C. Somers, S. B. Nelson, M. Sur, An emergent model of orientation selectivity in cat visual cortical simple cells. *The Journal of neuroscience : the official journal of the Society for Neuroscience* **15**, 5448-5465 (1995).
87. C. van Vreeswijk, H. Sompolinsky, Chaos in neuronal networks with balanced excitatory and inhibitory activity. *Science* **274**, 1724-1726 (1996).
88. C. van Vreeswijk, H. Sompolinsky, Chaotic balanced state in a model of cortical circuits. *Neural Comput* **10**, 1321-1371 (1998).

89. D. Hansel, C. van Vreeswijk, The mechanism of orientation selectivity in primary visual cortex without a functional map. *The Journal of neuroscience : the official journal of the Society for Neuroscience* **32**, 4049-4064 (2012).
90. T. W. Troyer, A. E. Krukowski, N. J. Priebe, K. D. Miller, Contrast-invariant orientation tuning in cat visual cortex: thalamocortical input tuning and correlation-based intracortical connectivity. *The Journal of neuroscience : the official journal of the Society for Neuroscience* **18**, 5908-5927 (1998).
91. T. W. Troyer, A. E. Krukowski, K. D. Miller, LGN input to simple cells and contrast-invariant orientation tuning: an analysis. *J Neurophysiol* **87**, 2741-2752 (2002).
92. G. C. DeAngelis, J. G. Robson, I. Ohzawa, R. D. Freeman, Organization of suppression in receptive fields of neurons in cat visual cortex. *J Neurophysiol* **68**, 144-163 (1992).
93. D. J. Heeger, Normalization of cell responses in cat striate cortex. *Vis Neurosci* **9**, 181-197 (1992).
94. M. Carandini, D. L. Ringach, Predictions of a recurrent model of orientation selectivity. *Vision Res* **37**, 3061-3071 (1997).
95. M. Carandini, D. J. Heeger, Summation and division by neurons in primate visual cortex. *Science* **264**, 1333-1336 (1994).
96. M. Carandini, D. J. Heeger, J. A. Movshon, Linearity and normalization in simple cells of the macaque primary visual cortex. *The Journal of neuroscience : the official journal of the Society for Neuroscience* **17**, 8621-8644 (1997).
97. T. Ohshiro, D. E. Angelaki, G. C. DeAngelis, A normalization model of multisensory integration. *Nat Neurosci* **14**, 775-782 (2011).
98. O. Ruiz *et al.*, Optogenetics through windows on the brain in the nonhuman primate. *J Neurophysiol* **110**, 1455-1467 (2013).
99. C. Stringer *et al.*, Spontaneous behaviors drive multidimensional, brainwide activity. *Science* **364**, eaav7893 (2019).
100. N. A. Steinmetz *et al.*, Neuropixels 2.0: A miniaturized high-density probe for stable, long-term brain recordings. *Science* **372**, eabf4588 (2021).
101. J. Hwang, A. R. Mitz, E. A. Murray, NIMH MonkeyLogic: Behavioral control and data acquisition in MATLAB. *Journal of Neuroscience Methods* **323**, 13-21 (2019).
102. R. J. Calin-Jageman, G. Cumming, Estimation for Better Inference in Neuroscience. *eneuro* **6**, ENEURO.0205-0219.2019 (2019).
103. J. Ho, T. Tumkaya, S. Aryal, H. Choi, A. Claridge-Chang, Moving beyond P values: data analysis with estimation graphics. *Nature Methods* **16**, 565-566 (2019).

Figure 1

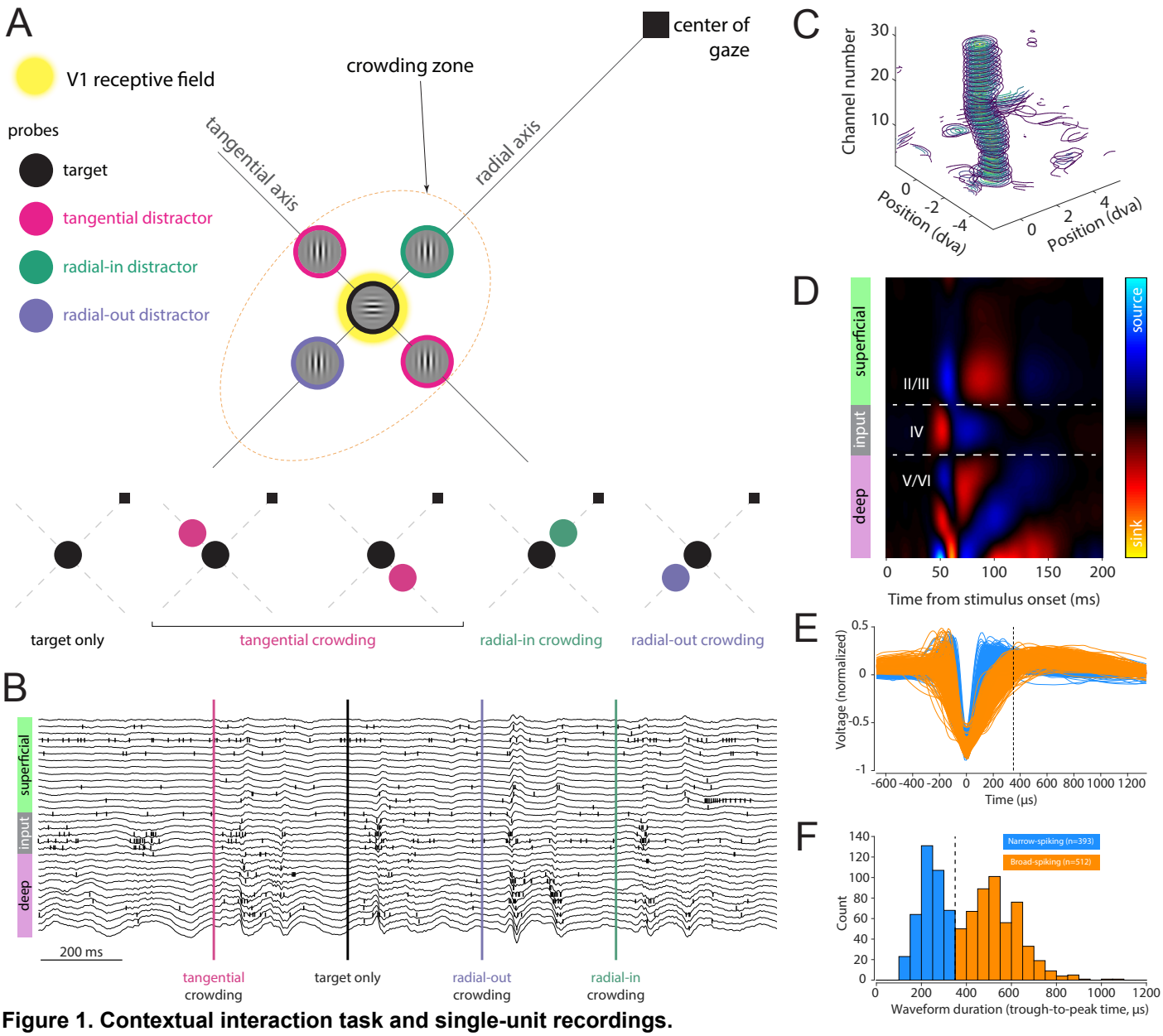

Figure 1. Contextual interaction task and single-unit recordings.
(**A**) Task schematic. Stimuli were presented alone at the receptive field center (target only) or with a distractor at one of the four locations surrounding the target. The radial axis connects the target to the center of gaze, and the tangential axis is orthogonal to it, also passing through the target. The top schematic shows stimuli at all possible locations, while the bottom section shows the possible spatial configurations for the presentation of an individual stimulus array. (**B**) Data recorded from a single trial, including spikes (black vertical ticks) and local field potentials (black traces) collected from each channel on one of the two shanks of the laminar probe. Data is arranged vertically based on the spatial location of the recording channel. Cortical layers are indicated on the left (green=superficial, gray=input, pink=deep). Vertical bars indicate the time of stimulus onsets. (**C**) Example receptive field contours vertically stacked for each recording site along the depth of a shank on the laminar probe. (**D**) Example current source density (CSD) map showing the early current sink (red) indicative of the input layer. (**E**) Mean waveforms for all recorded single-units (blue=narrow-spiking, orange=broad-spiking). (**F**) Distribution of waveform durations (trough-to-peak time) for all recorded single-units across the two monkeys. Neurons with waveform durations less than 350µs were classified as narrow-spiking (blue), and neurons with waveform durations greater than 350µs were classified as broad-spiking (orange).

Figure 2

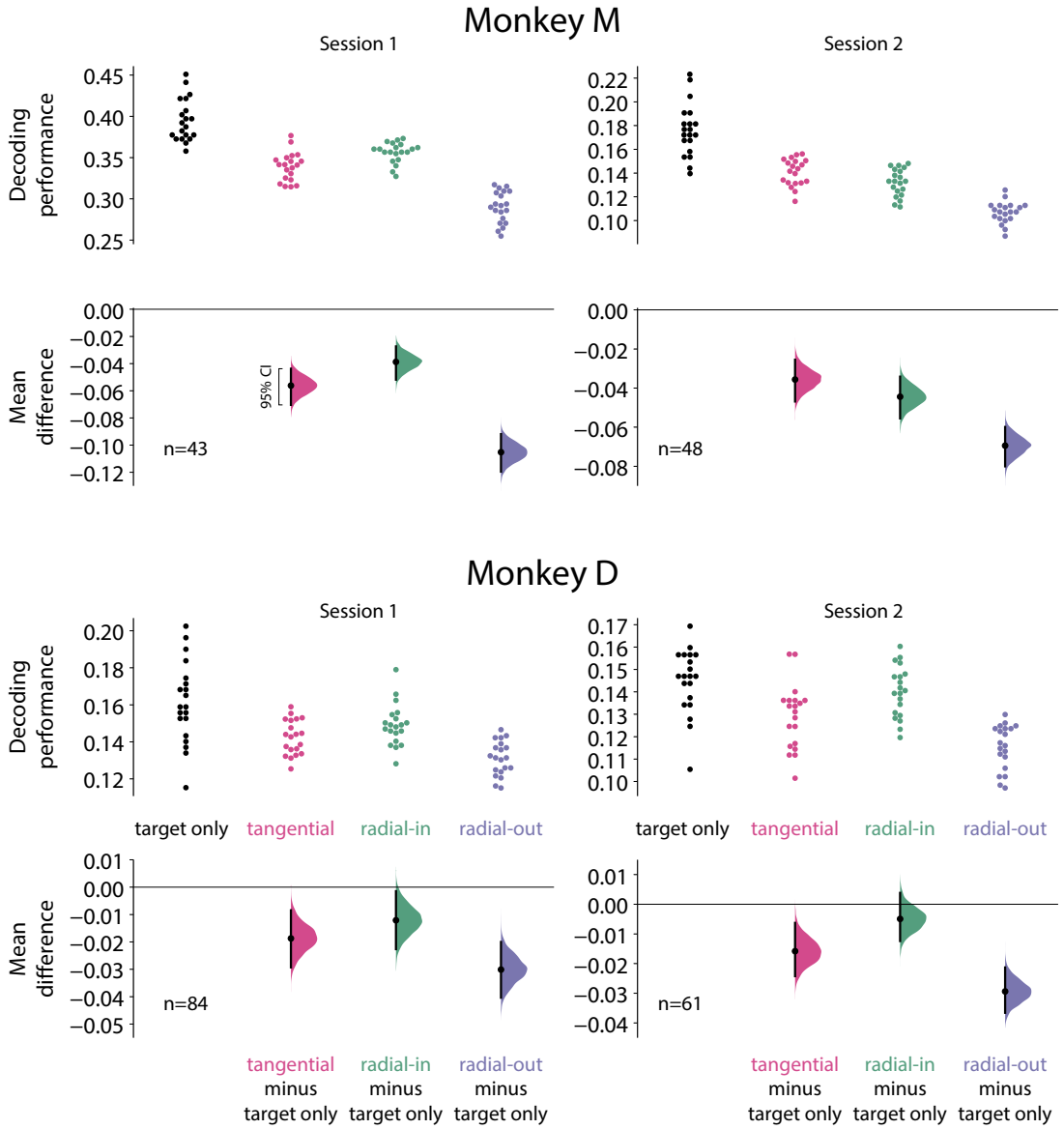

Figure 2. Distractor stimuli impair decoding performance in simultaneously recorded populations in an anisotropic manner.

Decoding performance from two example sessions in each monkey in the target-only condition and each of the three crowding conditions. Points in the upper section of each plot show the decoding performance for each of the 20 different cross-validations. The lower section for each session shows the bootstrapped estimation of the difference between decoding performance in each crowding condition compared to the target-only condition. Half-violin plots show the bootstrapped distribution of the difference, and black dots and bars represent the mean and 95% confidence intervals of the difference in decoding performance.

Figure 3

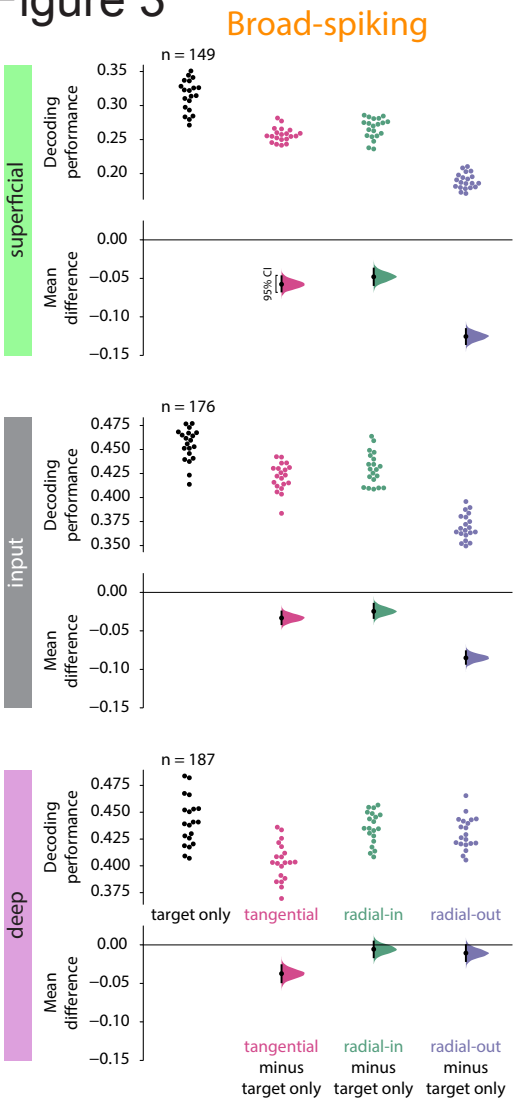

Figure 3. Radial-out crowding most strongly impairs decoding in the feed-forward pathway.
Decoding performance from broad-spiking neurons in each layer in the target-only condition and each of the three crowding conditions. Points in the upper section of each plot show the decoding performance for each of the 20 different cross-validations. The lower section for each layer shows the bootstrapped estimation of the difference between decoding performance in each crowding condition compared to the target-only condition. Half-violin plots show the bootstrapped distribution of the difference, and black dots and bars represent the mean and 95% confidence intervals of the difference in decoding performance.

Figure 4

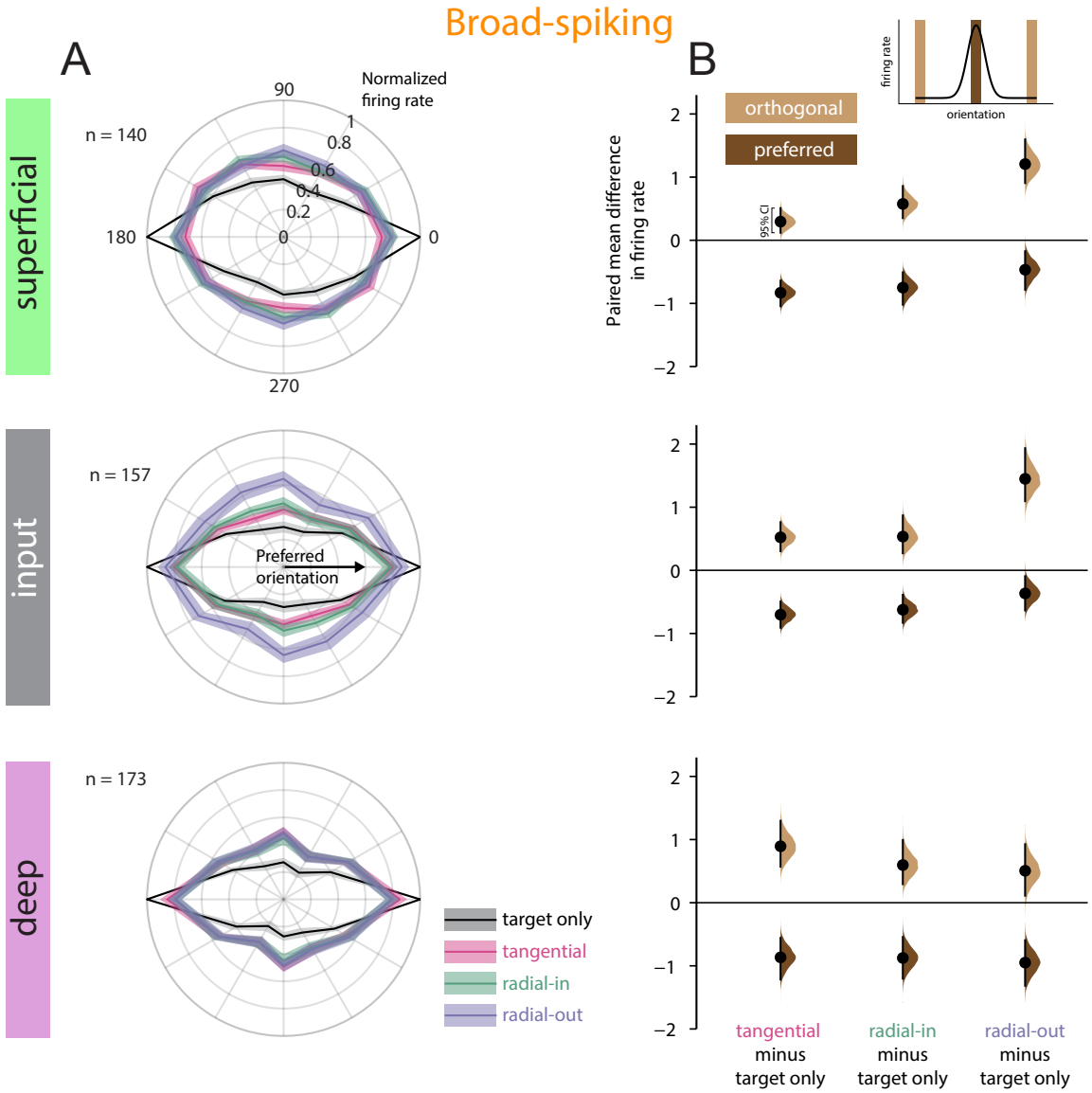

Figure 4. Crowding stimuli modulate the tuning curves of V1 neurons.
(**A**) Normalized tuning curves for broad-spiking neurons in each layer in the target-only and crowding conditions. Tuning curves are aligned with the preferred orientation at 0 degrees and duplicated to fill the circle. Tuning curves were normalized by the maximum firing rate in the target-only condition. Lines and shading represent mean +/- s.e.m. (black=target only, pink=tangential crowding, green=radial-in crowding, purple=radial-out crowding). (**B**) Difference in firing rate in response to preferred (dark brown) and orthogonal (light tan) stimuli under each crowding condition across layers. Colored half-violin plots show the bootstrapped estimation of the paired mean difference in firing rate for a given subpopulation, crowding condition, and stimulus orientation. Black dots and lines represent the mean and 95% confidence interval of the estimated difference.

Figure 5

Broad-spiking

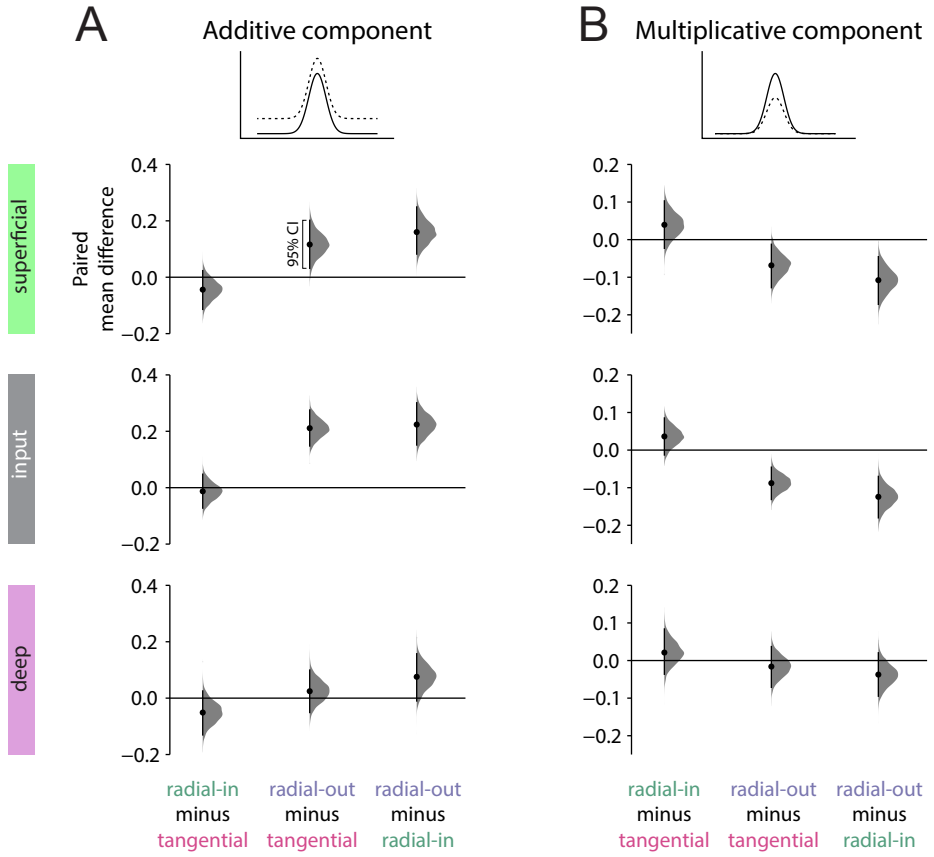

Figure 5. Radial-out crowding causes stronger additive facilitation and divisive suppression of tuning curves. (**A**) Difference in the modeled (see Methods) untuned additive facilitation of tuning curves of broad-spiking neurons caused by each of the crowding conditions. Gray half-violin plots show the bootstrapped estimation of the paired mean difference in the modeled additive component for a given subpopulation and pair of crowding conditions. Black dots and lines represent the mean and 95% confidence interval of the estimated difference. (**B**) Same as (**A**) but for the multiplicative component, reflecting tuned divisive suppression.

Figure 6

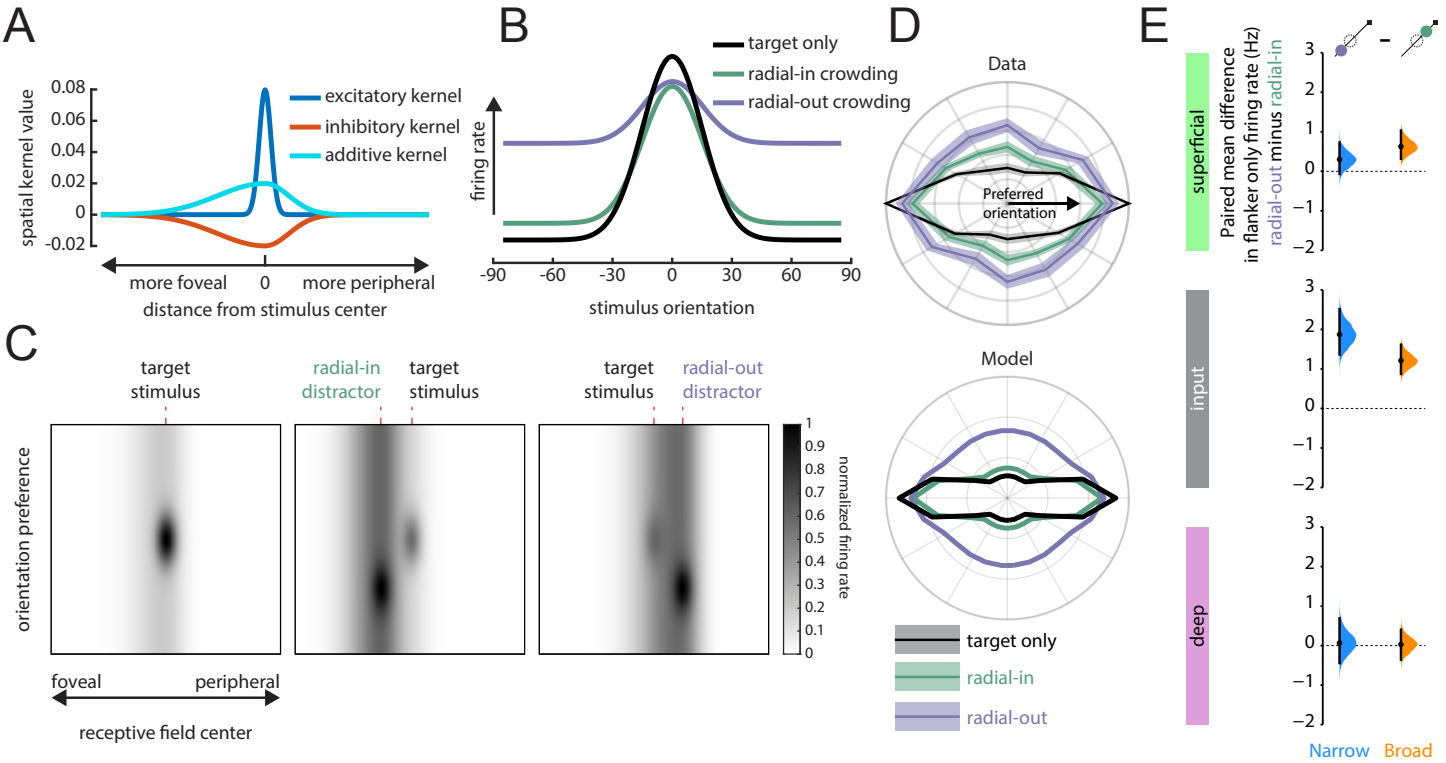

Figure 6. Normalization model with spatially skewed additive and divisive components explains crowding anisotropy.
(**A**) Excitatory (blue), inhibitory (red), and additive (cyan) kernels used in the normalization model. The additive and inhibitory kernels are skewed by doubling their standard deviation in the foveal direction and scaling both sides to maintain a smooth curve. (**B**) Modeled tuning curves in the target only (black), radial-in crowding (green), and radial-out crowding (purple). (**C**) Modeled population response in the three conditions: target only (left), radial-in crowding (middle), and radial-out crowding (right). (**D**) Comparison of population-averaged tuning curves from input-layer broad-spiking neurons (top, same as Figure 4A) and modeled tuning curves (bottom). (**E**) Difference in firing rate for each of the six subpopulations when a flanking stimulus was presented alone in the radial-out position compared to the radial-in position without the target present. Black dots and lines represent the mean and 95% confidence interval of the estimated difference.

Figure S1

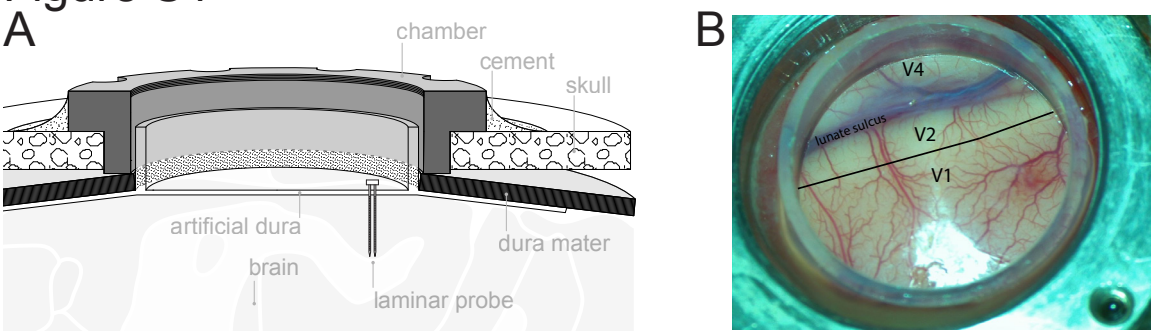

Figure S1. Laminar recordings in V1.
(**A**) Section perspective schematic of the artificial dura recording chamber and laminar probe. (**B**) Photo of the artificial dura chamber in one monkey.

Figure S2

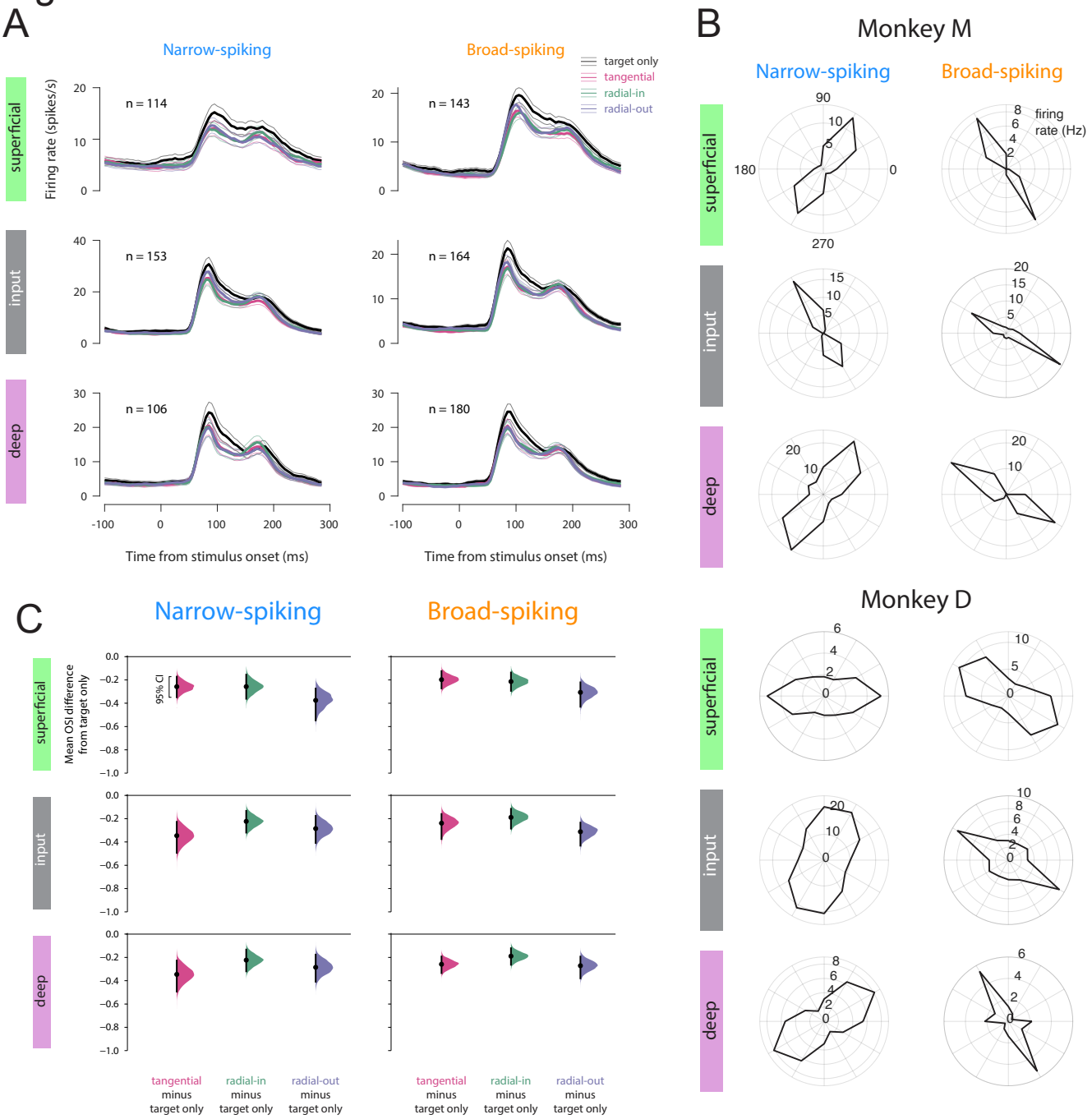

Figure S2. Peri-stimulus time histograms, tuning curves of single units, and orientation selectivity index under crowding.

(**A**) Peri-stimulus time histogram (PSTH) of subpopulations in each condition following the onset of the preferred stimulus. The preferred orientation was calculated separately for each single unit. Spikes were counted in 30ms bins shifted by 5ms. Error bars show mean+/- s.e.m. (**B**) Example single unit tuning curves in the target-only condition. Single units were selected from multiple different recording sessions. (**C**) Difference in orientation selectivity index (OSI) in each of the crowding conditions compared to the target-only condition. Colored half-violin plots show the bootstrapped estimation of the mean difference in OSI for a given subpopulation and crowding condition. Black dots and lines represent the mean and 95% confidence interval of the estimated difference.

Figure S3

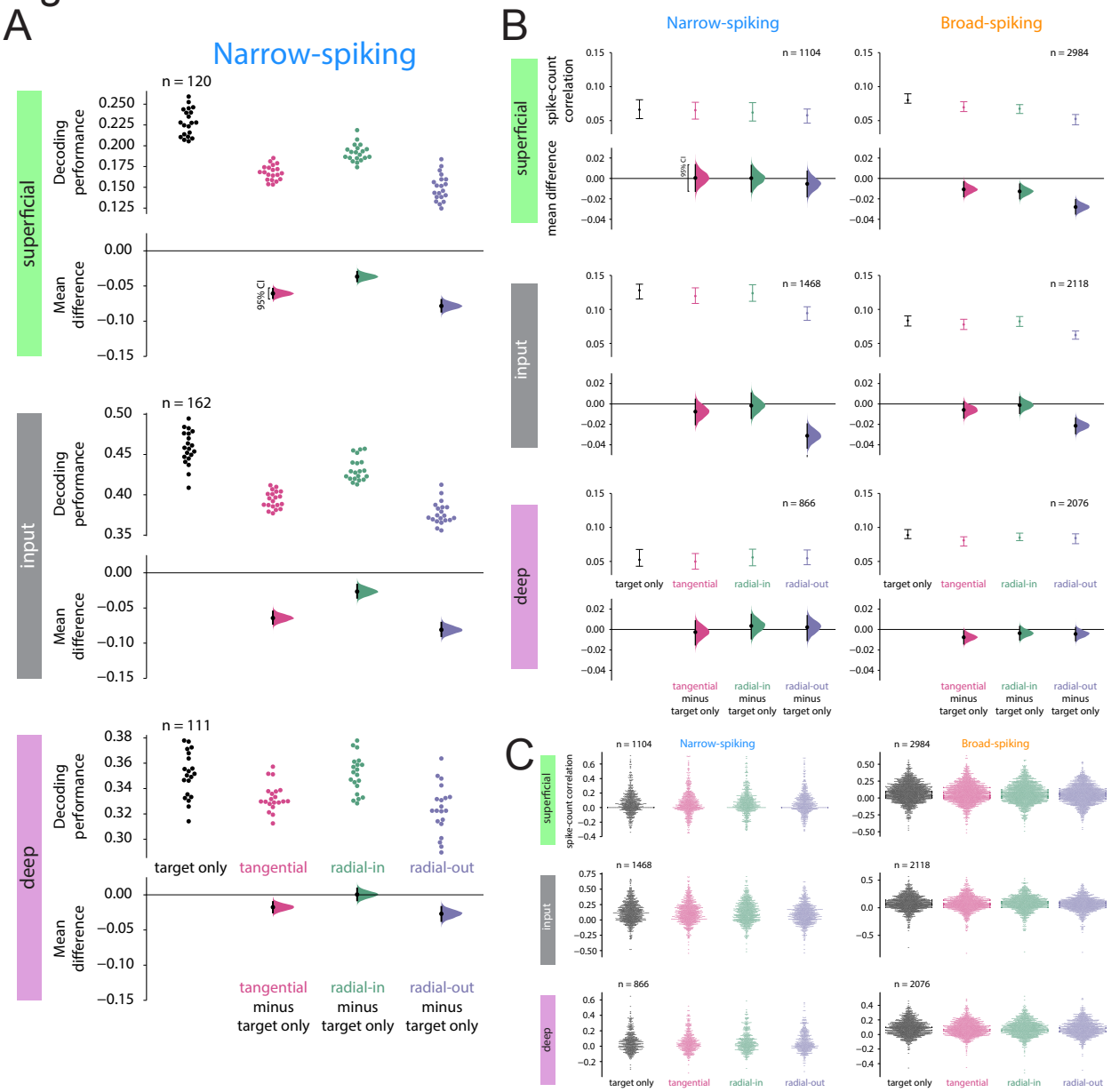

Figure S3. Decoding performance in narrow-spiking neurons and spike-count correlations
(**A**) Decoding performance from narrow-spiking neurons in each layer in the target-only condition and each of the three crowding conditions. Points in the upper section of each plot show the decoding performance for each of the 20 different cross-validations. The lower section for each layer shows the bootstrapped estimation of the difference between decoding performance in each crowding condition compared to the target-only condition. Half-violin plots show the bootstrapped distribution of the difference, and black dots and bars represent the mean and 95% confidence intervals of the difference in decoding performance. (**B**) Spike-count correlations from pairs of simultaneously recorded neurons in each subpopulation in the target-only condition and each of the three crowding conditions. In the top panels, error bars represent mean +/- 95% confidence intervals of the spike-count correlation in each condition. In the bottom panels, black dots and lines represent the mean and 95% confidence interval of the estimated difference from the target-only condition, and colored half-violin plots show the bootstrapped estimation of the mean difference in spike-count correlation for a given subpopulation and crowding condition. (**C**) Spike-count correlations for each pair of single units in each subpopulation. Each point represents the spike-count correlations of one pair of simultaneously recorded neurons in the same layer and cell class and each condition.

Figure S4

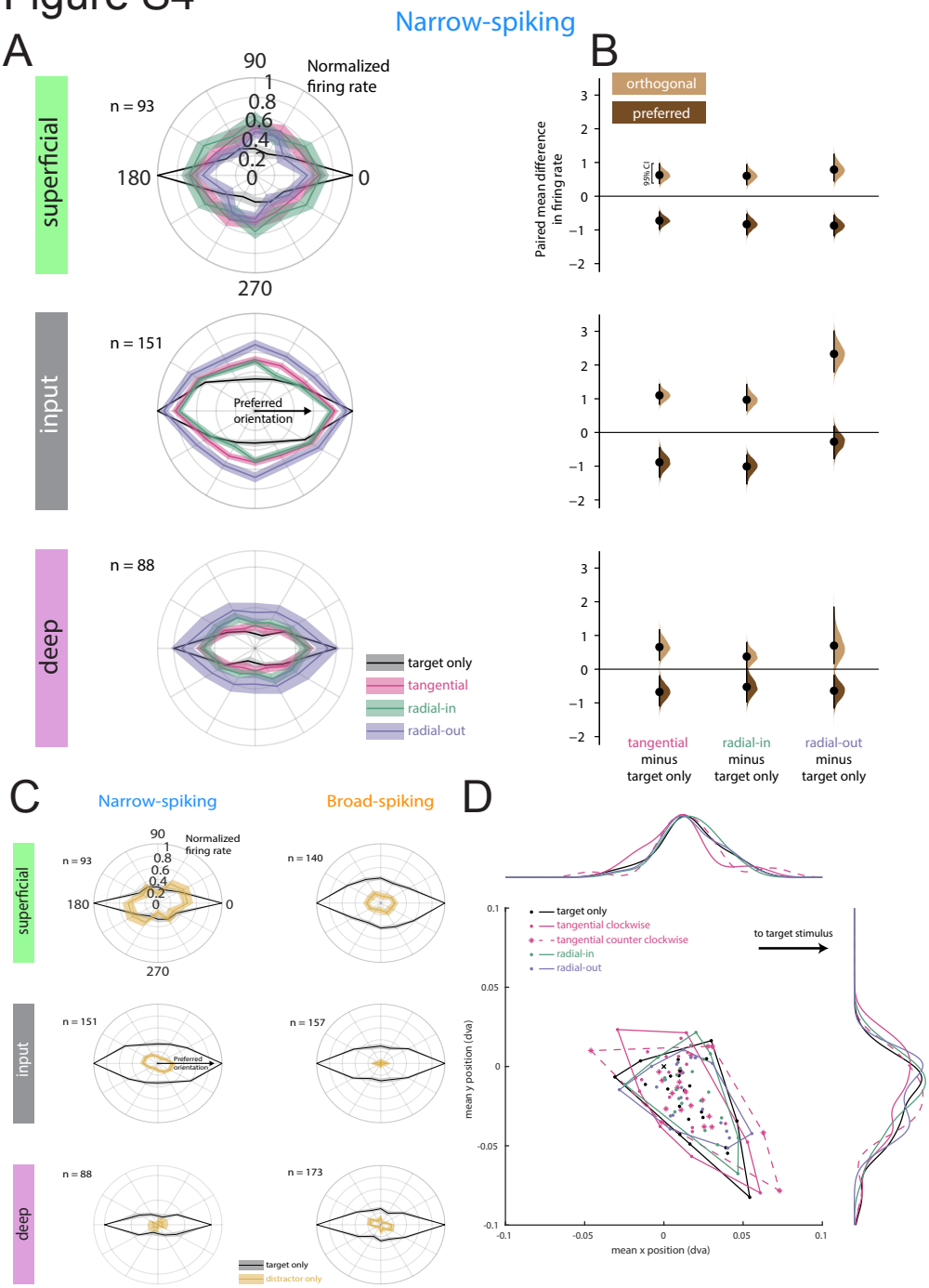

Figure S4. Tuning curves of narrow-spiking neurons, responses to flanker only, and eye position data.

(**A**) Normalized tuning curves for narrow-spiking neurons in each layer in the target-only and crowding conditions. Tuning curves are aligned with the preferred orientation at 0 degrees and duplicated to fill the circle. Tuning curves were normalized by the maximum firing rate in the target-only condition. Lines and shading represent mean +/- s.e.m. (black=target only, pink=tangential crowding, green=radial-in crowding, purple=radial-out crowding). (**B**) Difference in firing rate in response to preferred (dark brown) and orthogonal (light tan) stimuli under each crowding condition among narrow spiking neurons in each layer. Colored half-violin plots show the bootstrapped estimation of the paired mean difference in firing rate for a given subpopulation, crowding condition, and stimulus orientation. Black dots and lines represent the mean and 95% confidence interval of the estimated difference. (**C**) Normalized tuning curves for each subpopulation in the target-only and distractor-only conditions. Tuning curves are aligned with the preferred orientation at 0 degrees and duplicated to fill the circle. Tuning curves were normalized by the maximum firing rate in the target-only condition. The distractor-only condition is plotted relative to the orientation of the distractor and combines data from all four distractor positions. Lines and shading represent mean +/- s.e.m. (black=target only, gold=distractor only). (**D**) Mean eye position during the four conditions in each recording session. Each session has five points plotted (target only, radial-in crowding, radial-out crowding, and tangential clockwise crowding as dots, tangential counter-clockwise as stars). Above and to the right are marginal distributions of the median x and y positions for each of the sessions in each condition (tangential counter-clockwise plotted as a dashed line). To account for different target positioning across sessions, all data are rotated such that the target stimulus is to the right.

Figure S5

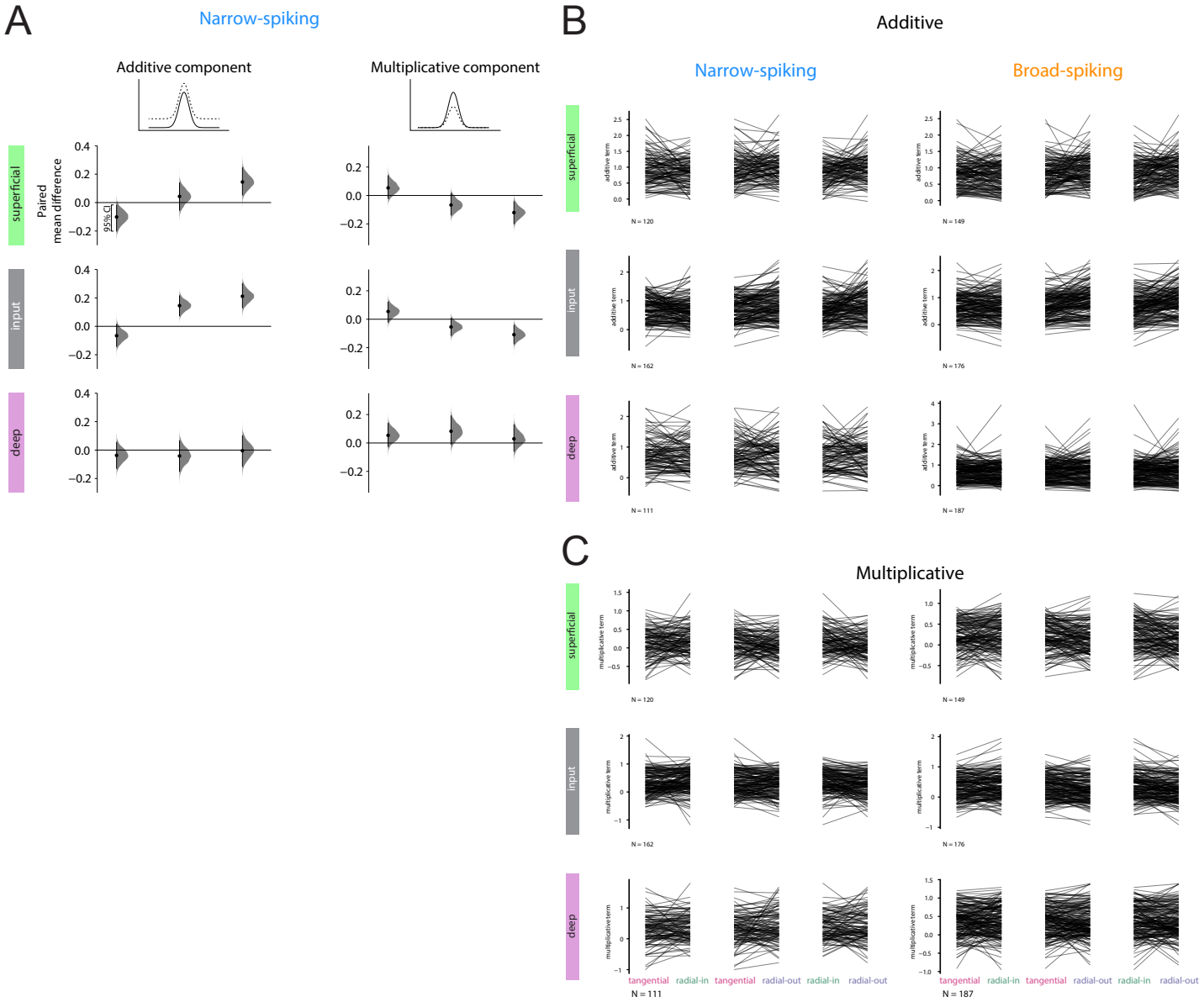

Figure S5. Single-unit tuning model parameters in different crowding conditions
(**A**) Difference in the modeled (see Methods) untuned additive facilitation (left) and multiplicative suppression (right) caused by each of the crowding conditions among narrow-spiking units. Gray half-violin plots show the bootstrapped estimation of the paired mean difference in the modeled additive component for a given subpopulation and pair of crowding conditions. Black dots and lines represent the mean and 95% confidence interval of the estimated difference. (**B**) Related to Figure 5A and S5A left. Value of the fitted additive parameter for each neuron in each crowding condition. Each line represents the additive parameter for a single unit in across the two crowding conditions indicated at the bottom. (**C**) Related to Figure 5B and S5A right. Same as (**B**) but for the multiplicative component.

Figure S6

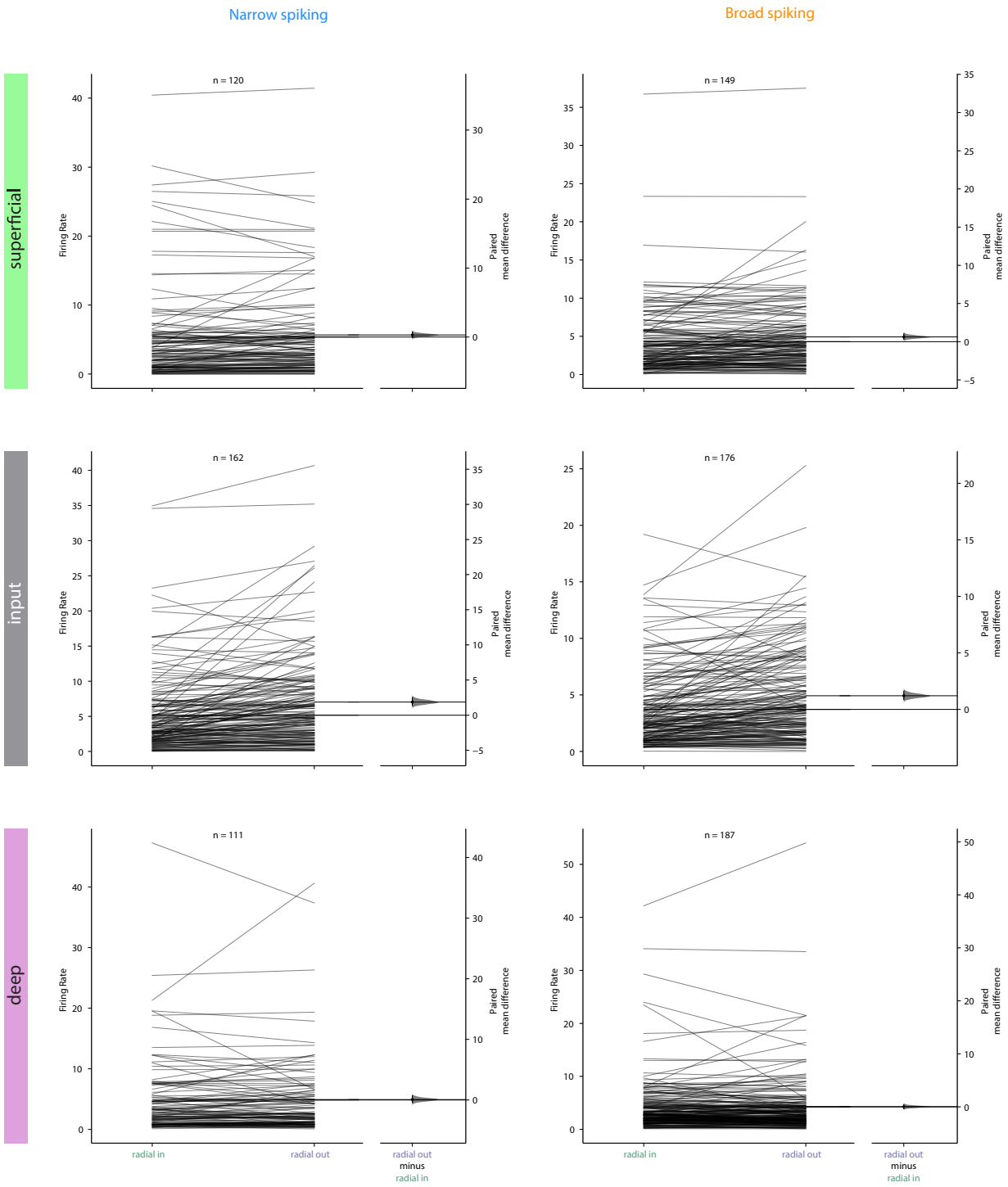

Figure S6. Single-unit firing rates in response to flanker alone
The average firing rate response of each neuron to stimuli in the radial-in or radial-out crowding position is shown on the left side of the plot for each subpopulation. On the right, gray half-violin plots show the bootstrapped estimation of the paired mean difference in firing rate for a given subpopulation and pair of crowding conditions. Black dots and lines represent the mean and 95% confidence interval of the estimated difference. Estimation statistics plots are the same as those in Figure 6E but scaled based on the raw firing rates shown here so that axes on the left and right are identical.